Microstructure-based multiscale modeling of large strain plastic deformation by coupling a full-field crystal plasticity-spectral solver with an implicit finite element solver

Fengbo Han [*], Franz Roters, Dierk Raabe

Max-Planck-Institut für Eisenforschung, Düsseldorf, Germany

ABSTRACT

We present a fully embedded implementation of a full-field crystal plasticity model in an implicit finite element (FE) framework, a combination which realizes a multiscale approach for the simulation of large strain plastic deformation. At each integration point of the macroscopic FE model a spectral solver, based on Fast Fourier Transforms (FFTs), feeds-in the homogenized response from an underlying full-field polycrystalline representative volume element (RVE) model which is solved by using a crystal plasticity constitutive formulation. Both, a phenomenological hardening law and a dislocation density based hardening model, implemented in the open source software DAMASK, have been employed to provide the constitutive response at the mesoscale. The accuracy of the FE-FFT model has been benchmarked by one-element tests of several loading scenarios for an FCC polycrystal including simple tension, simple compression, and simple shear. The multiscale model is applied to simulate four application cases, i.e., plane strain deformation of an FCC plate, compression of an FCC cylinder, four-point bending of HCP bars, and beam bending of a dual-phase steel. The excellent capabilities of the model to predict the microstructure evolution at the mesoscale and the mechanical responses at both macroscale and mesoscale are demonstrated.

1. Introduction

Crystal plasticity (CP) models based on the direct description of the kinematics and kinetics of the discrete and anisotropic deformation modes of metallic materials such as dislocation slip and mechanical twining have been successfully applied in predicting the mechanical response from the single crystalline up to the industrially relevant component scale (Kalidindi et al., 1992; Van Houtte et al., 2005; Roters et al., 2010, 2019; Van Bael et al., 2010; Helm et al., 2011). When simulating the response of parts and processes at macroscopic dimensions typically a homogenization approach within the Finite Element Method (FEM) is used rather than the direct full-field CP based simulation of a polycrystalline aggregate consisting of a typically prohibitively large number of grains. Three types of homogenization schemes are commonly used in such modeling scenarios, namely, full-field homogenization, mean-field homogenization, and grain-cluster homogenization (Roters et al., 2010).

Full-field homogenization refers to the spatially resolved solution of a representative volume element (RVE) by means of FEM (Smit et al., 1998; Miehe et al., 1999; Feyel and Chaboche, 2000; Kouznetsova et al., 2001; Kouznetsova et al., 2002; Miehe et al., 2002;

Feyel, 2003; Kouznetsova et al., 2004; Kouznetsova and Geers, 2008; Temizer and Wriggers, 2008; Geers et al., 2010; Larsson and Runesson, 2011; Temizer and Wriggers, 2011; Coenen et al., 2012; Reis and Andrade Pires, 2013) or spectral methods using a fast Fourier transform approach (FFT) (Moulinec and Suquet, 1998; Lebensohn, 2001; Spahn et al., 2014; Kochmann et al., 2016). Such a full-field homogenization approach can reach high precision in microstructure-property simulations when using adequate CP constitutive models and realistic microstructural morphologies. When compared to experiments, full-field CP simulations were found to work particularly well for multi-phase materials with their characteristic high mechanical contrast (Tasan et al., 2014a, 2014b; 2015; Diehl et al., 2016, 2017). However, among the existing full-field homogenization approaches, most still employ isotropic constitutive models to describe heterogeneous materials at the mesoscale rather than a CP model. Though CP models have been used in recent studies (Kochmann et al., 2016, 2018a, 2018b), they are limited to the small strain kinematical framework.

In mean-field homogenization approaches, the microstructure is represented in a statistical way where each grain is considered to be homogeneous, thus disregarding realistic microstructural in-grain morphologies and specific local grain interactions. Only spatially averaged quantities can be obtained instead of the spatially resolved solutions. Several models were developed along this line. The full constrained Taylor (1938) model is based on the iso-strain assumption, and was incorporated in early works, e.g. (Asaro and Needleman, 1985; Mathur and Dawson, 1989; Kalidindi et al., 1992; Beaudoin et al., 1993; Kalidindi, 1998), as well as in more recent works, e.g., (Jung et al., 2013; Zecevic et al., 2015b, a; Ardeljan et al., 2016; Fan et al., 2018; Lu et al., 2019). The viscoplastic self-consistent model (VPSC) (Molinari et al., 1987; Lebensohn and Tomé, 1993) takes into account the long-range interactions of grains embedded in a homogeneous effective medium, and was frequently applied in conjunction with FEM (Kaschner et al., 2001; Tomé et al., 2001; Walde and Riedel, 2007b, a; Segurado et al., 2012; Knezevic et al., 2013a; Knezevic et al., 2013b; Galán et al., 2014; Prakash et al., 2015; Knezevic et al., 2016; Zecevic et al., 2016; Zecevic and Knezevic, 2018). Also, elasto-plastic self-consistent (EPSC) (Turner and Tomé, 1994) models have been implemented in implicit FEM simulations (Zecevic et al., 2017; Zecevic and Knezevic, 2017, 2019).

Grain-cluster homogenization is an intermediate approach between the mean-field scheme and the full-field scheme. The degrees of freedom are restricted to a small number of regions (which are identified with grains or parts of grains) with homogeneous strain inside each zone. Direct neighbor-neighbor interactions among the constituents of a (multiphase) polycrystal are taken into account, so that approximate strain compatibility and stress equilibrium are achieved. Models along this line include the Grain Interaction (GIA) (Crumbach et al., 2006a, b), the (A)LAMEL (Van Houtte et al., 1999, 2002, 2005; Delannay et al., 2002), the Relaxed Grain Cluster (RGC) models (Eisenlohr et al., 2009; Tjahjanto et al., 2009b, a; Roters et al., 2010; Tjahjanto et al., 2015; Roters et al., 2019) and Relaxed Constraints Taylor-type models (Raabe, 1995; Raabe et al., 2002; Zhao et al., 2004).

When utilizing the homogenization schemes outlined above, the CP model is called during each increment of the macroscopic FE model and returns the homogenized stress response, which means that the CP model is directly embedded in the FE model. This approach is fundamentally different from some of the established hierarchical multiscale schemes (Van Houtte et al., 2006; Van Bael et al., 2010; Gawad et al., 2013, 2015; He et al., 2014, 2015; Han et al., 2019). In the latter schemes, the CP model is employed to conduct separately virtual experiments for calculating specific elastic-plastic anisotropy data. These stand-alone results are then used to identify and/or update parameters of an anisotropic yield surface function at the macroscopic FE level. An update is not necessarily requested during each increment of the FE model, instead, the update is done only if a certain criterion is satisfied, e.g. the accumulated plastic strain exceeds 0.05 since the last update. Hierarchical schemes are computational less costly while directly embedded models are more accurate.

In this paper, we present a multiscale model by directly embedding a full-field CP-spectral solver in an implicit finite element simulation. The implementation of the model is based on ABAQUS implicit (Dassault Systèmes, 2017) and DAMASK (Roters et al., 2019). The latter includes a spectral solver using Fast Fourier Transforms (FFTs) (Eisenlohr et al., 2013; Shanthraj et al., 2015; Wong et al., 2016; Zhang et al., 2016, 2018; Wang et al., 2018), which is very efficient in dealing with full-field CP problems with periodic boundary conditions. As various CP constitutive models have been implemented in DAMASK, all of these formulations are available in this multiscale framework. A phenomenological constitutive model and a dislocation density based constitutive model are employed in this work to test the new fully integrated multiscale model. Simple tension, simple compression, and simple shear tests are conducted to demonstrate the accuracy of the multiscale model (referred to as FE-FFT or ABAQUS-DAMASK) by comparing the results with those obtained directly from stand-alone DAMASK simulations. Subsequently, the multiscale model is applied to simulate four application cases, i.e. plane strain deformation of an FCC plate, compression of an FCC cylinder, four-point bending of an HCP bar, and beam bending of a dual-phase steel. The excellent capabilities of the model to predict microstructure evolution and mechanical response are demonstrated.

2. Finite strain crystal plasticity models and spectral method

The finite strain framework employed in DAMASK defines a deformation field $\boldsymbol{\chi}(\mathbf{x}) : \mathbf{x} \in \mathscr{B}_0 \to \mathbf{y} \in \mathscr{B}_t$, which maps points $\mathbf{x}$ in the reference configuration $\mathscr{B}_0$ to points $\mathbf{y}$ in the current configuration $\mathscr{B}_t$. The deformation gradient is given as $\mathbf{F} = \partial \boldsymbol{\chi} / \partial \mathbf{x}$, and its multiplicative decomposition reads as $\mathbf{F} = \mathbf{F}_e \mathbf{F}_p$. $\mathbf{F}_p$ is the plastic deformation gradient that maps to the plastic configuration, and $\mathbf{F}_e$ is the elastic deformation gradient that maps from the plastic to the deformed configuration.

2.1. Phenomenological constitutive model

The phenomenological constitutive model adopted in the present work follows the widely used power law first described by

Hutchinson (1976) for FCC crystals and then extended to also account for twinning by Kalidindi (1998). The shear on each slip system is described in rate form

$$\dot{\gamma}^{\alpha} = \left(1 - f_{\mathrm{tw}}^{\mathrm{tot}}\right)\dot{\gamma}_0^{\alpha}\left|\frac{\tau^{\alpha}}{g^{\alpha}}\right|^{1/m}\mathrm{sgn}(\tau^{\alpha}) \tag{1}$$

where $f_{\mathrm{tw}}^{\mathrm{tot}}$ is the total twin volume fraction, $\dot{\gamma}_0^{\alpha}$ is the reference strain rate for slip systems, τ^{α} is the resolved shear stress, g^{α} is the slip resistance, and m is the strain rate sensitivity exponent.

Accounting for the unidirectional character of twin formation, the shear on a twin system is handled in a slightly different way by

$$\dot{\gamma}^{\beta} = \left(1 - f_{\mathrm{tw}}^{\mathrm{tot}}\right)\dot{\gamma}_0^{\beta}\left|\frac{\tau^{\beta}}{g^{\beta}}\right|^{1/m}\mathscr{H}(\tau^{\beta}) \tag{2}$$

where $\mathscr{H}$ is the HEAVISIDE or unit step function.

The total twin volume fraction is given by

$$f_{\mathrm{tw}}^{\mathrm{tot}} = \min\left(\underbrace{\sum_{\beta=1}^{N_{\mathrm{tw}}} \gamma^{\beta}/\gamma_{\mathrm{char}}^{\beta}}_{=f_{\mathrm{tw}}^{\beta}},\ 1.0\right) \tag{3}$$

where $\gamma_{\mathrm{char}}^{\beta}$ is the characteristic shear of twin system β.

The evolution of the resistance on a slip system is given by

$$\dot{g}^{\alpha} = h_0^{\mathrm{s-s}}\left(1 + c_1\left(f_{\mathrm{tw}}^{\mathrm{tot}}\right)^{c_2}\right)\left(1 + h_{\mathrm{int}}^{\alpha}\right)\sum_{\alpha'=1}^{N_{\mathrm{s}}}|\dot{\gamma}^{\alpha'}|\left|1 - \frac{g^{\alpha'}}{g_{\infty}^{\alpha'}}\right|\mathrm{sgn}\left(1 - \frac{g^{\alpha'}}{g_{\infty}^{\alpha'}}\right)h^{\alpha\alpha'} + \sum_{\beta'=1}^{N_{\mathrm{tw}}}\dot{\gamma}^{\beta'}h^{\alpha\beta'} \tag{4}$$

where $h^{\alpha\alpha'}$ and $h^{\alpha\beta'}$ are the slip-slip and slip-twin interaction matrices respectively, $h_0^{\mathrm{s-s}}$, c_1, and c_2 are fitting parameters, and g_{∞} is the saturation value of the slip resistance.

The evolution of the resistance on a twin system is given in a similar way by

$$\dot{g}^{\beta} = h_0^{\mathrm{tw-s}}\left(\sum_{\alpha=1}^{N_{\mathrm{s}}}|\gamma^{\alpha}|\right)^{c_3}\sum_{\alpha'=1}^{N_{\mathrm{s}}}|\dot{\gamma}^{\alpha'}|h^{\beta\alpha'} + h_0^{\mathrm{tw-tw}}\left(f_{\mathrm{tw}}^{\mathrm{tot}}\right)^{c_4}\sum_{\beta'=1}^{N_{\mathrm{tw}}}\dot{\gamma}^{\beta'}h^{\beta\beta'} \tag{5}$$

where $h_0^{\mathrm{tw-s}}$, $h_0^{\mathrm{tw-tw}}$, c_3, and c_4 are fitting parameters.

2.2. Dislocation density based constitutive model

The dislocation density-based constitutive model follows the approach proposed by Ma and Roters (2004), which directly describes the processes of dislocation multiplication, dislocation annihilation, and dipole formation.

The shear rate of a slip system is given by the OROWAN equation

$$\dot{\gamma} = \rho b_{\mathrm{s}} v_0 \exp\left[-\frac{Q_{\mathrm{s}}}{k_B T}\left(1 - \left(\frac{|\tau_{\mathrm{eff}}|}{\tau_{\mathrm{sol}}}\right)^p\right)^q\right]\mathrm{sgn}(\tau) \tag{6}$$

where ρ is the dislocation density, b_{s} is the length of the Burgers vector, v_0 is a reference dislocation velocity, Q_{s} is the activation energy for dislocation slip, k_B is the BOLTZMANN constant, T is the temperature, τ_{sol} is the solid solution strength, p and q are fitting parameters controlling the strength of the glide resistance profile. τ_{eff} is the effective resolved shear stress, which is computed as

$$\tau_{\mathrm{eff}} = \begin{cases} |\tau| - \tau_{\mathrm{pass}} & \text{for } \tau > \tau_{\mathrm{pass}} \\ 0 & \text{for } \tau \leq \tau_{\mathrm{pass}} \end{cases} \tag{7}$$

where the dislocation passing stress τ_{pass} is given by

$$\tau_{\mathrm{pass}}^{\alpha} = Gb_{\mathrm{s}}^{\alpha}\left(\sum_{\alpha'=1}^{N_{\mathrm{s}}}h^{\alpha\alpha'}\left(\rho^{\alpha'} + \rho_{\mathrm{di}}^{\alpha'}\right)\right)^{1/2} \tag{8}$$

where G is the shear modulus and ρ_{di} is the dislocation dipole density.

The evolution of the (unipolar) dislocation density is given by

$$\dot{\rho} = \frac{|\dot{\gamma}|}{b_{\mathrm{s}}\Lambda_{\mathrm{s}}} - \frac{2\widehat{d}}{b_{\mathrm{s}}}\rho|\dot{\gamma}| \tag{9}$$

where Λ_s is the mean free path for dislocation slip.

The evolution of the dislocation dipole density is given by

$$\dot{\rho}_{di} = \frac{2(\widehat{d} - \breve{d})}{b_s}\rho|\dot{\gamma}| - \frac{2\breve{d}}{b_s}\rho_{di}|\dot{\gamma}| - \rho_{di}\frac{4v_{cl}}{\widehat{d} - \breve{d}} \tag{10}$$

The dislocation climb velocity is given by

$$v_{cl} = \frac{GD_0 V_{cl}}{\pi(1-\nu)k_B T}\frac{1}{\widehat{d} + \breve{d}}\exp\left(-\frac{Q_{cl}}{k_B T}\right) \tag{11}$$

where D_0 is the pre-factor of the self-diffusion coefficient, V_{cl} is the activation volume for dislocation climb, and Q_{cl} is the activation energy for climb.

Two dislocations will annihilate if the glide plane distance is smaller than the value $\breve{d}$, which is calculated as

$$\breve{d} = D_a b_s \tag{12}$$

where D_a is a fitting parameter.

They will form a stable dipole if the glide plane distance is larger than $\breve{d}$ but not larger than the value $\widehat{d}$, which is calculated as

$$\widehat{d} = \frac{3Gb_s}{16\pi|\tau|} \tag{13}$$

The mean free path for dislocation slip, Λ_s, has confining contributions due to the pileup of dislocations in front of grain boundaries and the dislocation-dislocation interaction, which is given by

$$\frac{1}{\Lambda_s^\alpha} = \frac{1}{D} + \frac{1}{i_s}\left(\sum_{\alpha'=1}^{N_{vw}}\xi^{\alpha\alpha'}\left(\rho^{\alpha'} + \rho_{di}^{\alpha'}\right)\right)^{1/2} \tag{14}$$

where D is the average grain size, i_s is a fitting parameter, and $\xi^{\alpha\alpha'}$ are projections for the forest dislocation density as introduced in (Ma and Roters, 2004).

2.3. Spectral method

The spectral method using the Fast FOURIER Transform (FFT) method to solve micromechanical boundary condition problems of heterogeneous materials usually exhibits a higher efficiency than the finite element method (FEM).

Considering a hexahedral microstructural domain $\mathscr{B}_0 \subset \mathbb{R}^3$ on which a macroscopic deformation gradient $\overline{\mathbf{F}}$ is imposed, the deformation map $\boldsymbol{\chi}(\mathbf{x})$ can be expressed as a sum of $\overline{\mathbf{F}}$ and a superimposed deformation fluctuation field $\tilde{\mathbf{w}}$,

$$\boldsymbol{\chi}(\mathbf{x}) = \overline{\mathbf{F}}\mathbf{x} + \tilde{\mathbf{w}}(\mathbf{x}) \tag{15}$$

for which periodic boundary conditions hold, i.e. $\tilde{\mathbf{w}}^- = \tilde{\mathbf{w}}^+$ on corresponding surfaces $\partial\mathscr{B}^-$ and $\partial\mathscr{B}^+$. Following Eq. (15), the total deformation gradient $\mathbf{F}$ is given by

$$\mathbf{F} = \overline{\mathbf{F}} + \tilde{\mathbf{F}} \tag{16}$$

The first PIOLA-KIRCHHOFF stress is expressed through a strain energy density functional $\mathscr{W}$:

$$\mathbf{P}(\mathbf{x}) = \frac{\delta\mathscr{W}}{\delta\mathbf{F}}(\mathbf{x}, \mathbf{F}, \zeta, \ldots) \tag{17}$$

where ζ is a set of evolving internal variables.

For an externally imposed average deformation, the equilibrium deformation field is obtained by minimizing $\mathscr{W}$ over all deformation fields that fulfill Eq. (15). Static equilibrium expressed in real and FOURIER space follows

$$\min_x \mathscr{W} \Rightarrow \text{Div}\mathbf{P}(\mathbf{x}) = \mathscr{F}^{-1}[\mathbf{P}(\mathbf{k})\,i\,\mathbf{k}] = 0 \tag{18}$$

which is equivalent to finding the root of the residual body force field

$$\mathscr{F}[\boldsymbol{\chi}(\mathbf{k})] := \mathbf{P}(\mathbf{k})\,i\,\mathbf{k} = 0 \tag{19}$$

Due to its high condition number, the differential Eq. (19) in FOURIER space is numerically difficult to solve. To tackle this problem, a linear homogeneous reference material of linear stiffness $\mathbb{D}$ is introduced, which transforms Eq. (19) into an equivalent problem (i.e. $\mathbf{P}(\mathbf{x}) = \mathbb{D}\mathbf{F}(\mathbf{x}) = \mathbb{D}\text{Grad}\boldsymbol{\chi}$) with better numerical properties. For a given deformation map $\boldsymbol{\chi}$, equilibrium in this reference material is fulfilled if the residual body force field vanishes
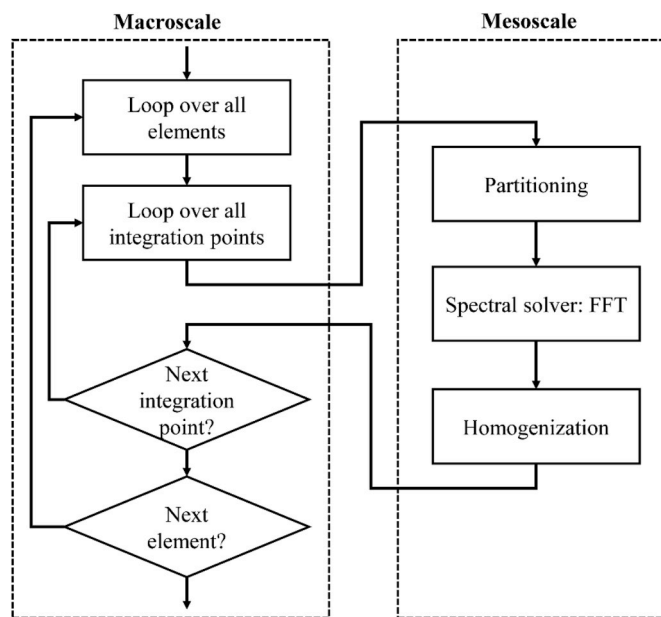
Fig. 1. Flow chart of the stages of the multiscale model embedding the spectral solver in FEM.
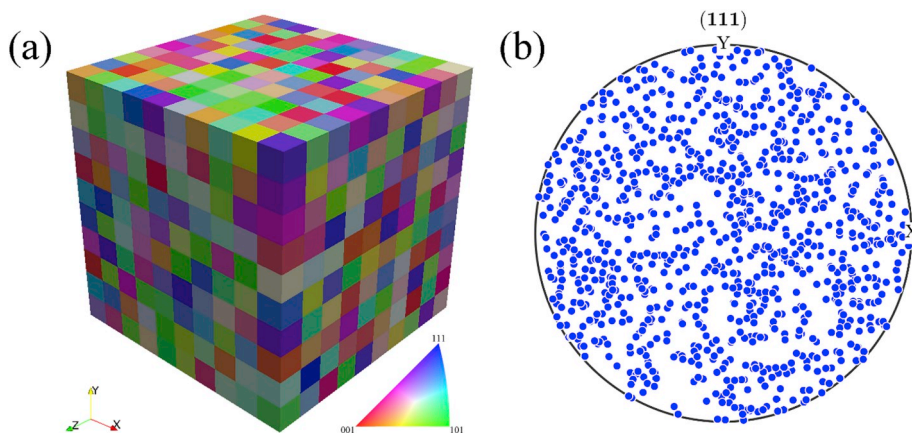

Fig. 2. (a) Representative volume element colored according to the inverse pole figure (IPF) along Z-direction (b) random texture assigned to the RVE (only one pole per orientation shown).

Table 1
Constitutive parameters used for the dislocation density based modeling of pure aluminum.

Symbol	Description	Value	Unit
C_{11}	Elastic constant	106.75	GPa
C_{12}		60.41	GPa
C_{44}		28.34	GPa
b_s	Burgers vector length	0.286	nm
ρ_{di}	Initial dipole density	1.0	m^{-2}
ρ	Initial dislocation density	$8.89 \cdot 10^{11}$	m^{-2}
Q_s	Activation energy for slip	$3.0 \cdot 10^{-19}$	J
v_0	Reference dislocation velocity	10^{-4}	$m \cdot s^{-1}$
τ_{sol}	Solid solution strength	5.07	MPa
p, q	Parameters for controlling the obstacle profile	1.0	
Q_{cl}	Activation energy for climb	$2.4 \cdot 10^{-19}$	J
V_{cl}	Activation volume for climb	$1.0(b_s)^3$ s	m^3
i_s	Fitting parameter	4.38	
D_a	Fitting parameter	29	
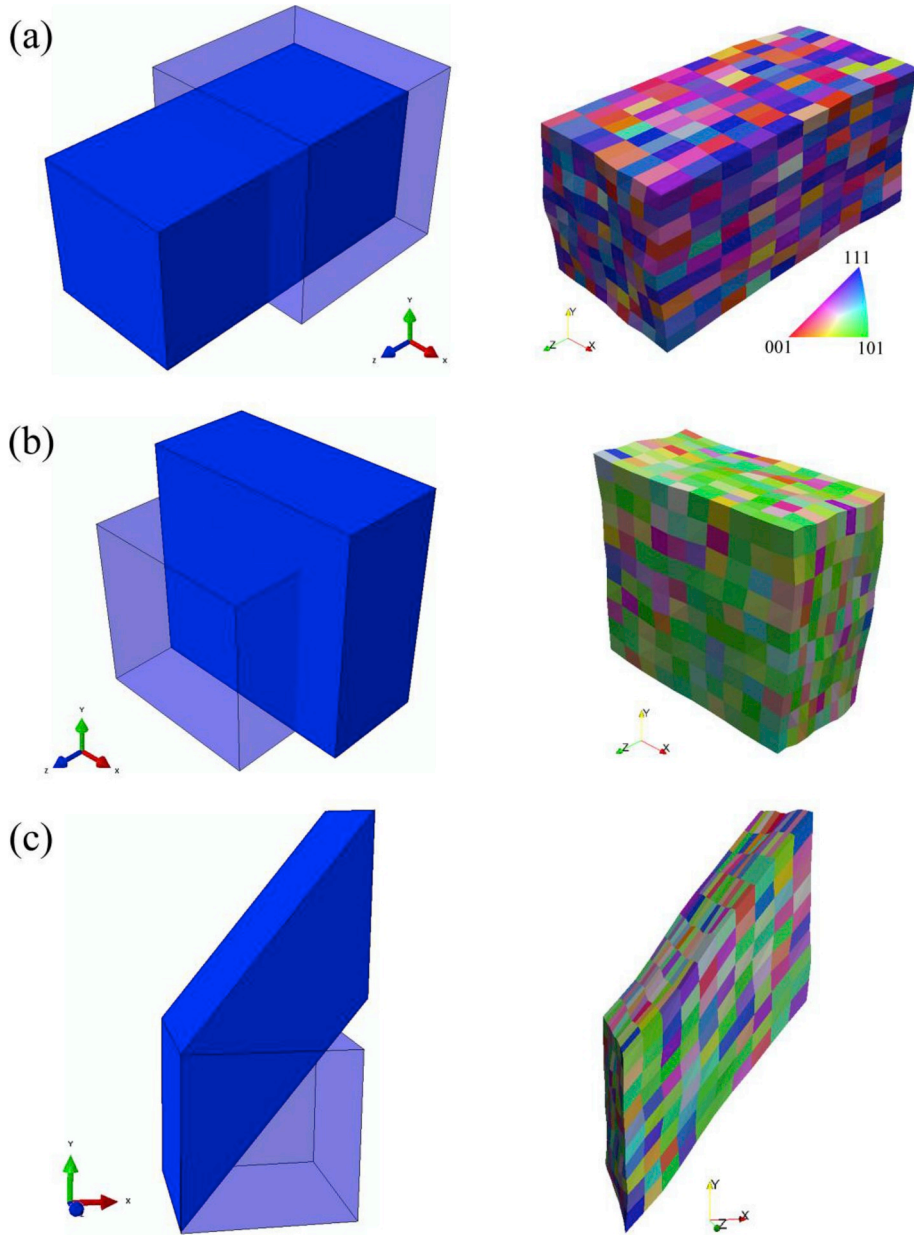
Fig. 3. One-element tests for (a) simple tension (b) simple compression (c) simple shear, showing the shapes of the single elements and the embedded RVE after deformation. The RVEs are colored according to the IPF along the reference Z-direction.

$$\mathscr{P}[\boldsymbol{\chi}(\mathbf{k})\,] := \mathbb{D}[\boldsymbol{\chi}(\mathbf{k}) \otimes i\,\mathbf{k}]\,i\,\mathbf{k} = \mathbf{A}(\mathbf{k})\boldsymbol{\chi}(\mathbf{k}) = 0 \tag{20}$$

The acoustic tensor $\mathbf{A}(\mathbf{k})$ corresponds to an operator on a deformation map producing the body forces resulting in the reference material. It is defined as $\mathbf{A}(\mathbf{k})\mathbf{a}(\mathbf{k}) := \mathbb{D}[\mathbf{a}(\mathbf{k}) \otimes i\,\mathbf{k}]\,i\,\mathbf{k}$ for any given vector field $\mathbf{a}(\mathbf{k})$. The inverse operator $\mathbf{A}^{-1}$ gives the deformation map that would result from a known body force field in the reference material. Thus it allows defining an operator that results in the deformation map causing the same body force field in the reference material as a given deformation map in the original material, which corresponds to a preconditioning operation of $\mathscr{P}^{-1}$ on the non-linear operator $\mathscr{F}$. The preconditioned system thus reads ($\forall \mathbf{k} \neq 0$):

$$\mathscr{P}^{-1}\mathscr{F}[\boldsymbol{\chi}(\mathbf{k})] = \mathbf{A}(\mathbf{k})^{-1}\mathbf{P}(\mathbf{k})\,i\,\mathbf{k} = 0 \tag{21}$$

The deformation gradient field corresponding to this deformation map is obtained as
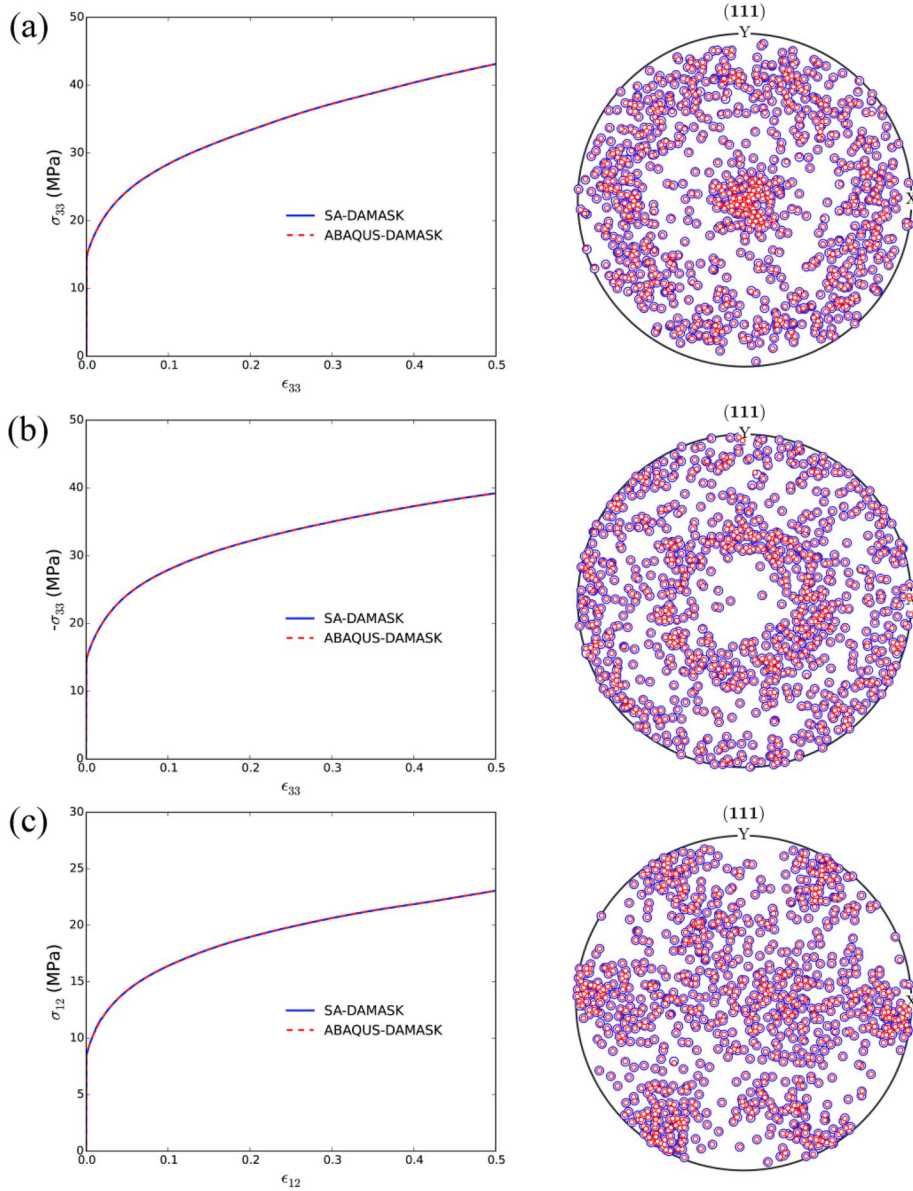
Fig. 4. Stress-strain curve and pole figure predictions of the multiscale model compared to the corresponding predictions obtained from a stand-alone (SA-) DAMASK simulation for (a) simple tension (b) simple compression (c) simple shear. Red circles in the pole figures represent the orientations predicted by the multiscale model while the blue ones represent those predicted by the stand-alone DAMASK simulation. (For interpretation of the references to color in this figure legend, the reader is referred to the Web version of this article.)

$$\mathscr{P}^{-1}\mathscr{F}[\boldsymbol{\chi}(\mathbf{k})] \otimes i\,\mathbf{k} = \left[\mathbf{A}(\mathbf{k})^{-1}\mathbf{P}(\mathbf{k})\,i\,\mathbf{k}\right] \otimes i\,\mathbf{k} = 0 \tag{22}$$

which is equivalent to Eq. (21) except for the case of $\mathbf{k} = 0$ where the prescribed average deformation gradient always holds. Eq. (22) can be expressed in FOURIER space in terms of the deformation gradient field as

$$\mathscr{F}_{\text{mech}}[\mathbf{F}(\mathbf{k})] := \boldsymbol{\Gamma}(\mathbf{k})\mathbf{P}(\mathbf{k}) = 0 \tag{23}$$

where the Gamma operator $\boldsymbol{\Gamma}(\mathbf{k})$ is defined as a shorthand notation to $\boldsymbol{\Gamma}(\mathbf{k})\mathbf{T}(\mathbf{k}) := [\mathbf{A}(\mathbf{k})^{-1}\mathbf{T}(\mathbf{k})\,i\,\mathbf{k}] \otimes i\,\mathbf{k}$ for a tensor field $\mathbf{T}(\mathbf{k})$. Eq. (23) is discretized by a collocation-based approach at the FOURIER points in the real space and it results in the system of equations

$$\mathscr{F}_{\text{basic}}[\mathbf{F}(\mathbf{x})] := \mathscr{F}^{-1}\left[\begin{cases} \boldsymbol{\Gamma}(\mathbf{k})\mathbf{P}(\mathbf{k}) & \text{for } \mathbf{k} \neq 0 \\ \Delta\mathbf{F} & \text{for } \mathbf{k} = 0 \end{cases}\right] \tag{24}$$
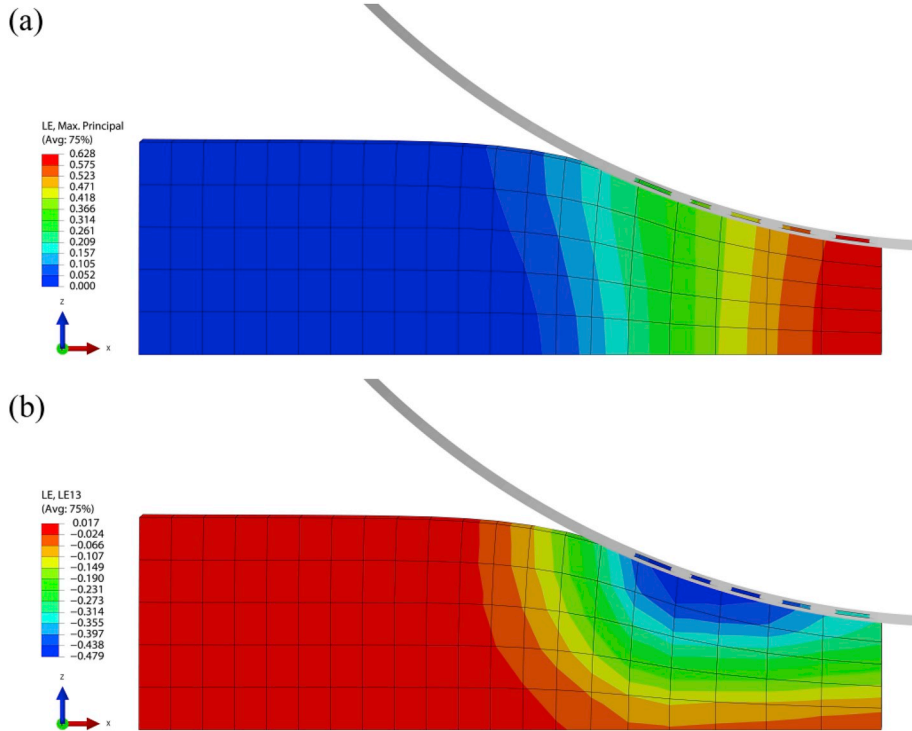
Fig. 5. ABAQUS-DAMASK simulation of plane strain deformation of pure Al with a round rigid die. Distributions of (a) maximum principal strain (b) shear strain component LE13.

3. Partitioning and homogenization

Fig. 1 shows a flow chart of the individual stages of the multiscale model and the workflow among them. At the macroscale, the FE model determines the evolution of the deformation gradient. A partitioning scheme is used to impose the deformation gradient on the RVE of the full-field CP model at the mesoscale. In the present approach, Eq. (15) reflects this scheme. This means that the deformation gradient from the FE integration point is passed to the RVE of DAMASK as the homogeneous part $\overline{\mathbf{F}}$. Following the full-field solution of the CP constitutive model using the spectral solver, simple volume averaging is used to obtain the average stress response, knowing the distribution of the microscopic stress field. The implicit FE code requires not only the input of the stress at the end of the time step but also the tangent stiffness matrix (Jacobian). As the spectral solver employed in the mesoscale uses fully implicit time stepping the local stiffness matrix is known. Thus the tangent stiffness matrix of the RVE can be directly retrieved by volume averaging.

It needs to be noted that in the standard version of DAMASK the stress field is explicitly given as a first PIOLA-KIRCHHOFF stress measure $\mathbf{P}$, and a transformation to the Cauchy stress measure $\boldsymbol{\sigma}$, as required by ABAQUS, can be achieved by applying $\boldsymbol{\sigma} = (\det\mathbf{F})^{-1}\mathbf{PF}^{\mathrm{T}}$. A transformation from the DAMASK tangent $\mathrm{d}\mathbf{P}/\mathrm{d}\mathbf{F}$ to the tangent matrix appropriate to the Jaumann rate of Cauchy stress has also to be done (see Appendix B for details).

4. Benchmark tests

The correctness of the implementation and accuracy of the multiscale model are first checked by comparing the results of the multiscale model (ABAQUS-DAMASK) against the results of the stand-alone DAMASK model in cases of simple boundary conditions. For the multiscale model, a simple FE model with a single linear element C3D8R is used, and a representative volume element (RVE) is embedded in the integration point. This procedure is referred to as single material point test.

The material used here is pure aluminum with random crystallographic texture. Fig. 2(a) shows the RVE which consists of $10 \times 10 \times 10$ FOURIER points. Each FOURIER point represents one grain, and the grain orientations are shown in the pole figure in Fig. 2(b). It needs to be noted that the pole figure just shows one dot per pole per grain. We decided to do so, as in the following, we are going to compare the crystallographic textures (represented as sets of individual grain orientations) predicted by the multiscale model with those obtained by the stand-alone DAMASK model in a pole figure on a one-to-one basis. In this case, the chosen representation limits the number of poles shown in the pole figures for better clarity. The dislocation density based constitutive model (section 2.2) is employed in the benchmark tests. The parameters of the constitutive model have been identified by using a genetic algorithm (Lin and Yang, 1999) based on an inverse optimization approach to reproduce the experimental single crystal tensile stress-strain behavior of aluminum (Hosford et al., 1960). The identified parameters for pure aluminum are listed in Table 1.
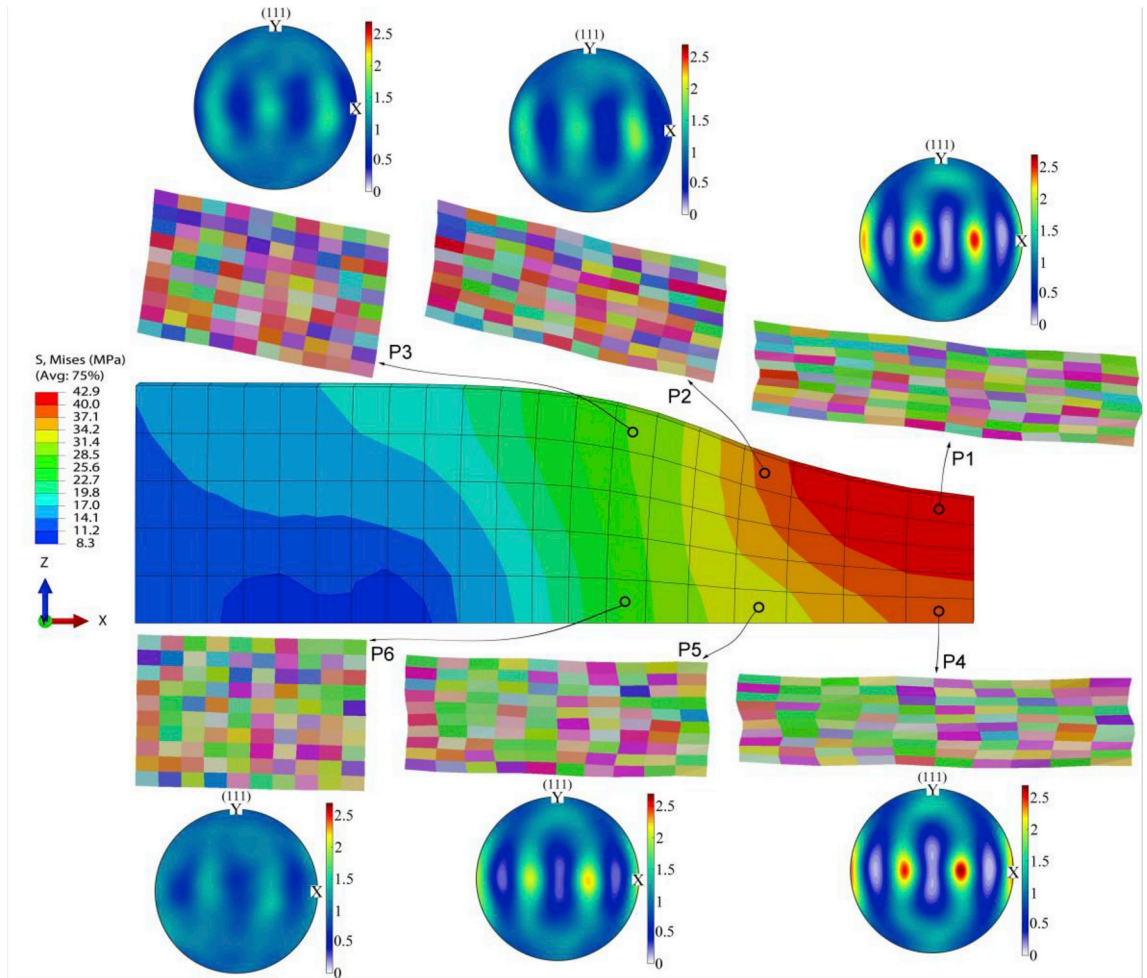
Fig. 6. ABAQUS-DAMASK simulation of plane strain compression of pure Al: Distribution of the Von Mises stress shown in the x-z plane, together with the final shapes of the embedded RVEs and corresponding crystallographic textures shown as pole figures projected in the x-y planes at the six positions indicated.

The shapes of the elements and the embedded RVEs after simple tension, simple compression, and simple shear are shown in Fig. 3 (a–c), respectively. In all three load cases, the embedded RVE deforms according to the boundary condition imposed by the single element of the macroscale FE model. The changes of the grain orientations at the mesoscale can be identified in terms of the color changes of the RVEs.

The stress-strain curves and pole figures predicted by the multiscale model are compared with those predicted by the stand-alone DAMASK for the three load cases in Fig. 4. Hardly any loss of accuracy can be observed regarding the prediction of the stress-strain response and the texture, indicating a very high accuracy of the implemented multiscale model.

5. Application examples

5.1. Plane strain deformation of a pure Al plate

Plane strain deformation of a pure Al plate with a round rigid die was simulated to further illustrate the capabilities of the multiscale model in complex deformation conditions. The initial size of the plate is 3×1 mm in the x-z plane. The mesh contains 100 C3D8R linear elements. A displacement of -0.5 mm in z-direction was imposed to the round die at a constant tool velocity of 5 mm s^{-1} to compress the plate. The friction coefficient is set to 0.3. The dislocation density based constitutive model as calibrated in section 4 is also employed in this simulation. Fig. 5 shows the final geometry and the strain distribution of the plate. A heterogeneous strain pattern ranging between 0.157 and 0.628 maximum principal strain evolves in the region under the contact surface. Large shear strains (with a maximum value of 0.479) occur in the region near the contact surface. Fig. 6 shows the distribution of the Von Mises stress, together with the final shapes of the embedded RVEs and corresponding textures at the six positions indicated. The shapes of the elements at these positions are consistent with those of the embedded RVEs. The three positions (P4, P5, and P6) located at the bottom of the plate
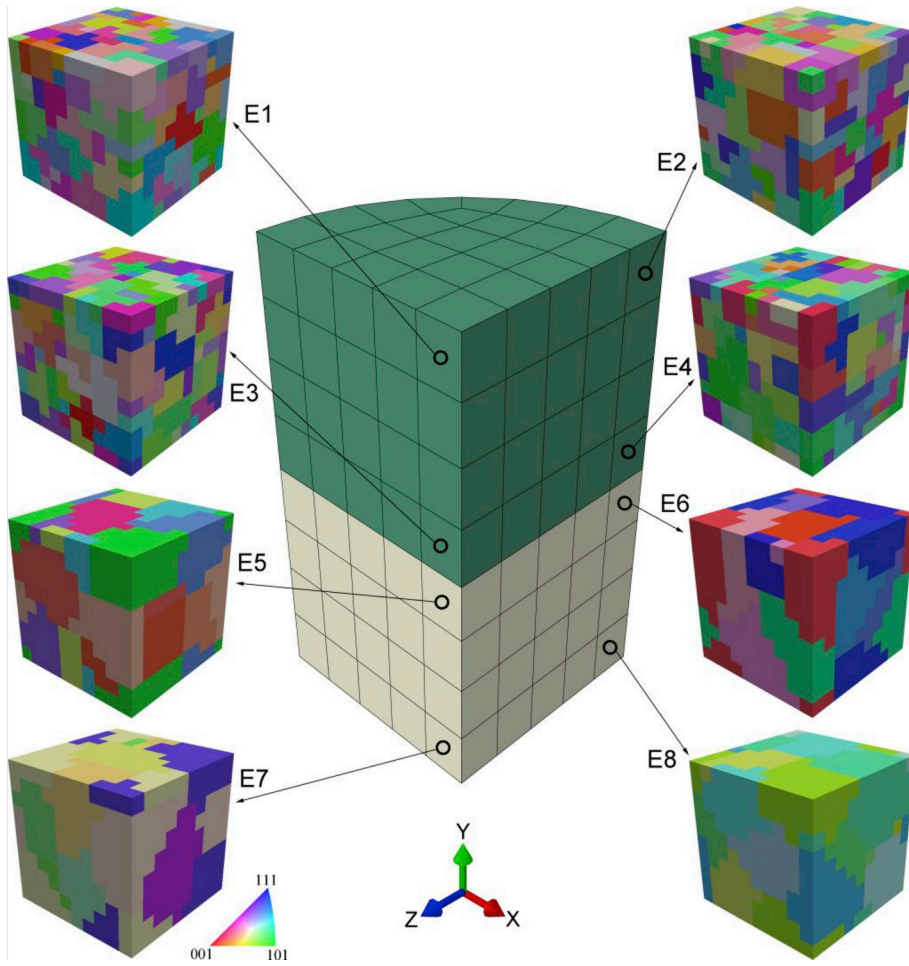
Fig. 7. FE model of a cylinder with different RVEs assigned at each integration point. The upper half of the cylinder assigned with fine-grained RVEs while the lower half assigned with coarse-grained RVEs. The RVEs are colored according to the IPF along Z-direction.

are in a nearly pure plane strain compression state, so that the elements and the embedded RVEs are just in a simple compression configuration as well. The other three positions (P1, P2, and P3) located in the region near the contact surface are in more complex deformation states including compression, shear, and rotation, so that the elements and the embedded RVEs at these positions are in more complex configurations as well. As a consequence of the different deformation histories in the region near the contact surface and the bottom region of the plate, the final textures in the two regions are distinctly different. Typical plane strain compression textures for FCC material (Hölscher et al., 1994; Raabe, 1995; Raabe et al., 2002) are found at the three positions (P4, P5, and P6) located at the bottom of the plate, as can be observed from the <111> pole figures. The highest texture intensity appears at position P4 where the largest compression strain is found. The textures at the positions near the contact surface (P1, P2, and P3) exhibit rotations with respect to the y-axis, which is a result of the complex deformation history. Evidently, all the results at the mesoscale are consistent with the results at the macroscale.

5.2. Compression of a pure Al cylinder

Next we study a more complex setup to consider microstructural statistics and heterogeneity at the macroscale. Fig. 7 shows a quarter FE model of a cylinder with different RVEs assigned at each integration point. The cylinder has a diameter of 1 mm and a height of 1 mm, discretized into a mesh with 192 C3D8R elements. For the upper half of the cylinder, the RVEs contain 100 grains, while the RVEs just contain 10 grains in the same dimension for the lower half of the cylinder. In other words, the upper half has a fine-grained microstructure while the lower half has a coarse-grained microstructure with the aim to mimic the effect of grain size heterogeneity. The Voronoi tessellation method is used to generate the geometries of the RVEs. The seeds of the Voronoi tessellation are randomly generated, and so are the grain orientations. In this way, each integration point of the macroscale FE model has an individual RVE so that the whole cylinder has sufficient statistical characteristics of the microstructure. Each RVE consists of a grid of $10 \times 10 \times 10$ points. The dislocation density based constitutive model is again used in this simulation.
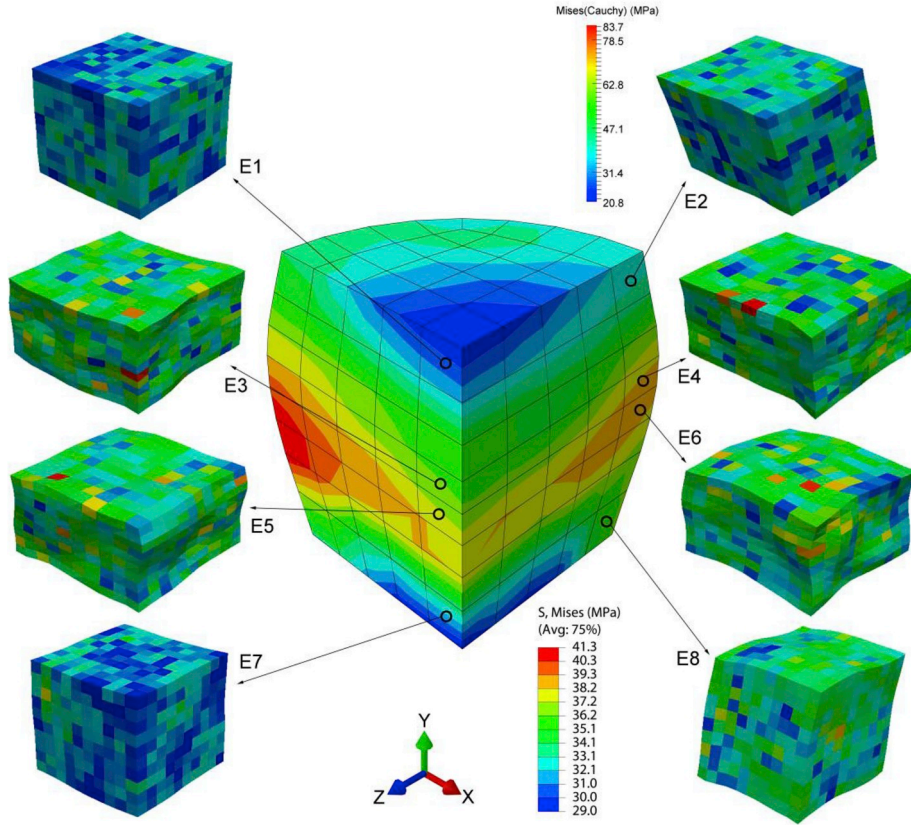
Fig. 8. ABAQUS-DAMASK simulation of the compression of an Al cylinder with heterogeneous microstrcture: Von Mises stress distribution of the deformed cylinder and that of the embedded RVEs at eight positions. The colorbar at the top is for the RVEs while that at the bottom is for the FE model.

The cylinder was compressed to 75% of its original height imposing a tool velocity of 0.1 mm s^{-1}. Fig. 8 depicts the Von Mises stress distribution of the deformed cylinder and that of the embedded RVEs at eight positions. Although the boundary conditions of the upper half and the lower half of the cylinder are symmetrical, the stress distribution in the cylinder is obviously asymmetrical. This can be ascribed to the use of individual RVEs for each integration point and the grain size heterogeneity of the upper and lower half of the cylinder. The stress distributions of the RVEs that result from grain-scale interactions are different from each other. The stress levels and the shapes of the eight embedded RVEs are consistent with those of the corresponding macroscale elements.

This example indicates that the present multiscale model is able to capture sufficient statistical information of the microstructure by employing multiple RVEs. In particular, it should be very effective to describe materials with large microstructure heterogeneity, such as sheet metals with texture gradients across the thickness direction (Tikhovskiy et al., 2006, 2008), materials with grain size gradients, and microstructures of welded joint.

### 5.3. Four-point bending of Zr bars

Two simulations of four-point bending of textured Zr bars were performed to evaluate the capability of the multiscale model to predict the directionality of twinning. To perform the four-point bending experiments (Kaschner et al., 2001; Tomé et al., 2001), 2 bars of square cross-section were cut from a clock-rolled Zr plate, then they were bent along different directions. In one case, the through-thickness direction (of the original plate) lies in the bending plane, i.e., the <c>-axes are mostly aligned in the bending plane, while in the other case, the through-thickness direction is perpendicular to the bending plane, i.e., the <c>-axes are mostly aligned perpendicular to the bending plane. The simulations follow the same settings as the experiments.

The phenomenological crystal plasticity constitutive model accounting for twinning (section 2.1) is employed. The slip and twinning modes consist of $\{10\bar{1}0\}\langle\bar{1}2\bar{1}0\rangle$ prismatic <a>, $\{0001\}\langle11\bar{2}0\rangle$ basal <a>, $\{10\bar{1}1\}\langle\bar{1}\bar{1}23\rangle$ pyramidal <c+a>, $\{10\bar{1}2\}\langle10\bar{1}1\rangle$ tensile twinning and $\{11\bar{2}2\}\langle11\bar{2}\bar{3}\rangle$ compressive twinning. An RVE of 1000 grains (with the resolution of $10 \times 10 \times 10$ FOURIER points) assigned with a texture sampled from the experimental texture (Kaschner et al., 2001; Tomé et al., 2001) was created to represent the material. Fig. 9 shows both, the experimentally observed texture and the corresponding texture reconstructed from the 1000 discrete orientations that had been assigned to the RVE. The hardening parameters were again identified by the genetic algorithm based inverse optimization approach to reproduce the experimental stress-strain curves of uniaxial in-plane tension, uniaxial in-plane
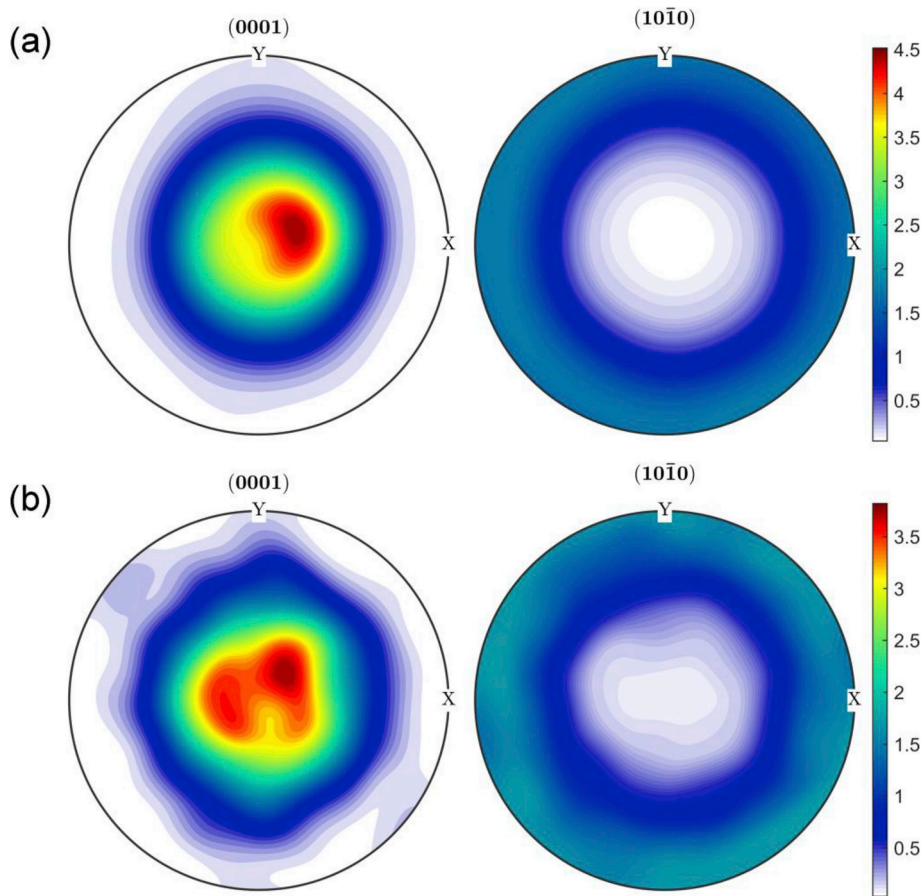
Fig. 9. Initial texture of Zr (a) experimental (Kaschner et al., 2001; Tomé et al., 2001) (b) reconstructed from 1000 discrete orientations that were assigned to the RVE.
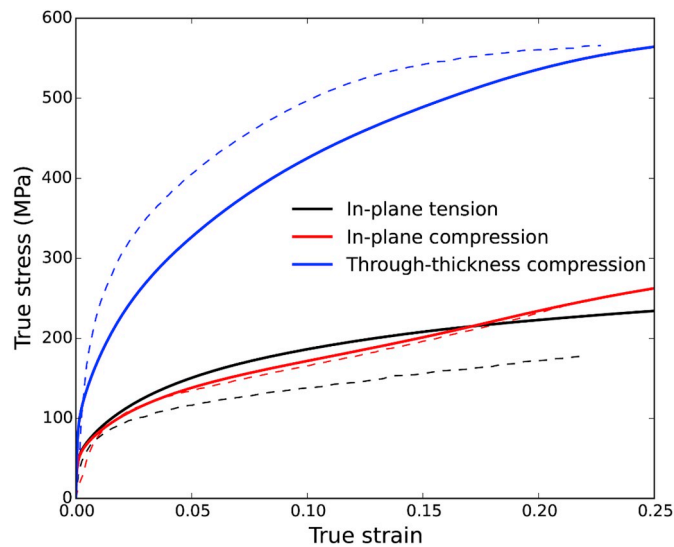
Fig. 10. Comparisons of experimental (—) and fitted (——) stress-strain curves of Zr. The experimental data were taken from the work of (Tomé et al., 2001).

Table 2
Constitutive parameters used for the phenomenological constitutive law to model Zr.

| Symbol	Description	Value	Unit
g_0^{pri}	Initial slip resistance of Prismatic <a>	13	MPa
g_0^{pri}	Initial slip resistance of basal <a>	32	MPa
g_0^{pyr}	Initial slip resistance of pyramidal <c+a>	345	MPa
g_∞^{pri}	Saturation slip resistance of Prismatic <a>	76	MPa
g_∞^{bas}	Saturation slip resistance of basal <a>	115	MPa
g_∞^{pyr}	Saturation slip resistance of pyramidal <c+a>	2134	MPa
$g_{tw,0}^{T}$	Initial tensile twinning resistance	90	MPa
$g_{tw,0}^{C}$	Initial compressive twinning resistance	531	MPa
h_0^{s-s}	Fitting parameter	718	MPa
h_0^{tw-tw}	Fitting parameter	3297	MPa
h_0^{tw-s}	Fitting parameter	3857	MPa
m	Strain rate sensitivity exponent	0.1	
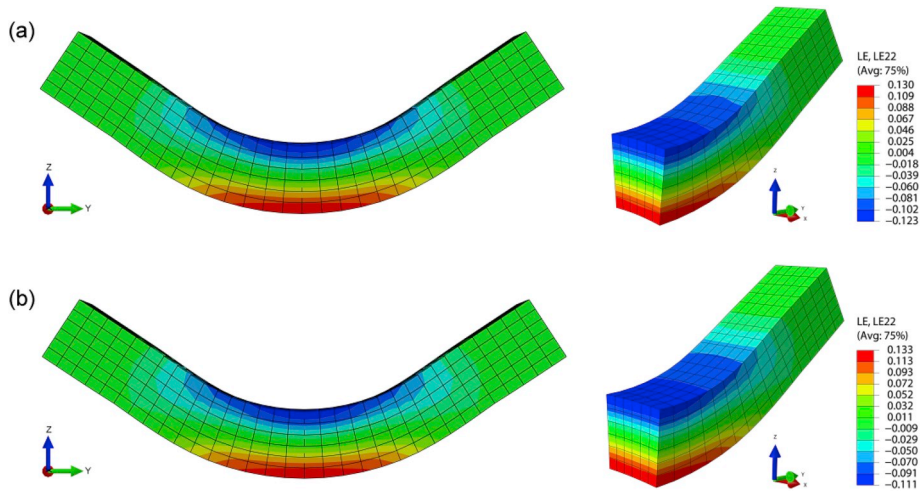
Fig. 11. Final shapes of the textured Zr bars after four-point bending (a) the through-thickness direction lies on the bending plane (b) the through-thickness direction is perpendicular to the bending plane.

compression and through-thickness compression of Zr as shown in Fig. 10. The parameters identified are listed in Table 2. It needs to be noted that the parameters were first optimized by fitting to the stress-strain curve of uniaxial in-plane compression to obtain a preliminary fit, then they were further optimized by fitting to all three curves in parallel. The stress-strain response reproduced by the fit has 18.2% deviation to the experimental values. Even though the fitting is not optimal it is considered sufficient for the purpose of this work, i.e. demonstrating the capabilities of the multiscale approach rather than validating the constitutive models used.

The four-point bending was conducted on a rectangular bar with initial dimensions 6.35 × 6.35 × 50.8 mm. Due to the orthotropic symmetry of the problem, only a quarter of the problem is modeled and symmetry boundary conditions are imposed. The bar was discretized using 288 reduced integration hexahedral elements (C3D8R). The upper pins and the lower pins were located at 6.35 mm and 19.05 mm from the midpoint, respectively. During bending, the lower pins were fixed while the upper pins were displaced 6 mm downward.

Fig. 11 shows the final shapes of the bars after four-point bending in the lateral and 3D views. Though the lateral views for the two cases are very similar to each other, differences can be observed from the 3D views as well as from the longitudinal strain distributions. From the 3D views, it can be seen that the lateral section of the bar with the through-thickness direction lying on the bending plane is more warped than that of the bar with the through-thickness direction perpendicular to the bending plane. This can be also observed more clearly from Fig. 12 which shows the simulated cross sections of the Zr bars after four-point bending together with the experimental ones (Kaschner et al., 2001). Since the through-thickness direction of the highly textured Zr bar is hard to deform, the plastic flow of the bar during deformation has strong directionality. When the through-thickness direction is aligned in the bending plane, the plastic deformation is localized in the x-y plane, resulting in a wedge-shaped cross section. When it is aligned perpendicular to the bending plane, the plastic flow in the x-y plane is limited, so the cross section keeps a more square shape. It can be also observed that the simulations are in good agreement with the experiments.
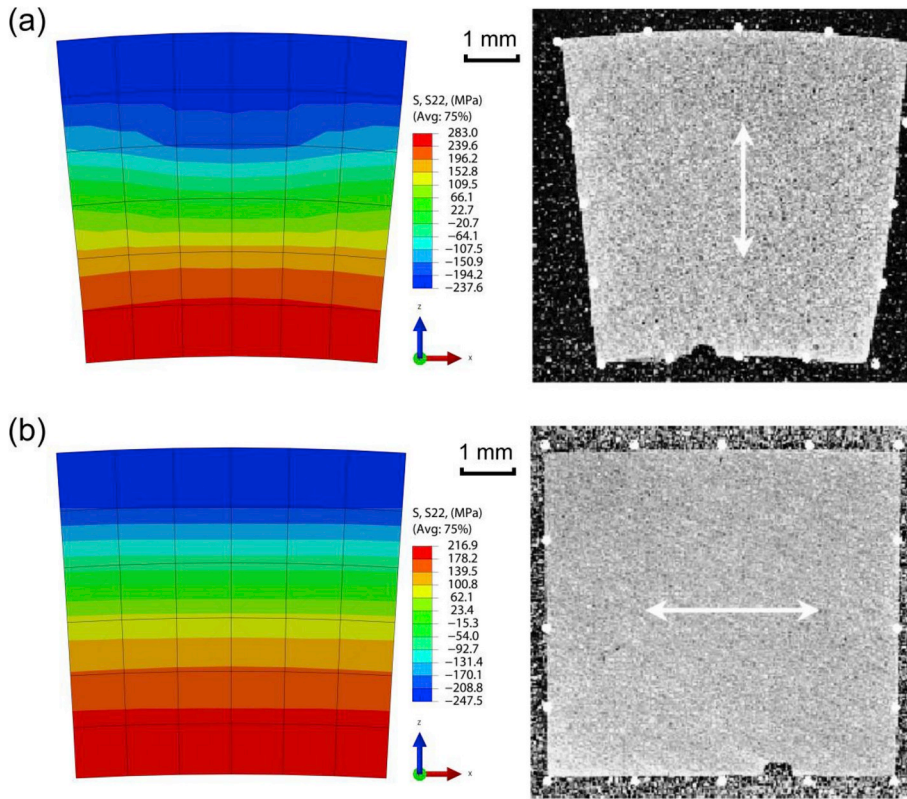
Fig. 12. Cross sections of the Zr bars after four-point bending (a) through-thickness direction lies on the bending plane (b) through-thickness direction is perpendicular to the bending plane to the bending plane. The left hand side images show the simulated results and the right hand side images show the experimental results. The experimental data were taken from the work of (Kaschner et al., 2001).

5.4. Beam bending of a dual-phase steel

To further demonstrate the ability of the multiscale model in simulations of materials with complex microstructure, a beam bending process was simulated, in which a high resolution dual-phase RVE was embedded in each FE integration point. Fig. 13(a) shows the mesh and the boundary conditions of the beam. The beam has a dimension of $1 \times 3 \times 7$ mm, and it was discretized using 21 C3D8R elements. During bending, one end of the beam was fixed, while two nodes of the other end were displaced by 1 mm downward. Here we aim to demonstrate the capabilities of the integrated RVE-FEM model approach for the case of a two phase material, hence we chose a ferritic-martensitic dual phase steel here (Tasan et al., 2015). Fig. 13(b) and (c) show the RVE with 100 grains (80 ferrite grains and 20 martensite grains) for the dual phase steel (Tasan et al., 2014a). The RVE has a high grid resolution of $64 \times 64 \times 64$ points. It needs to be noted that the RVE has been created here for demonstration purposes, but the grain size ratio between ferrite and martensite may be not realistic. The phenomenological power law included in the DAMASK distribution is used here. The parameters for ferrite and martensite phase used in the simulation can be found in (Tasan et al., 2014b).

Fig. 14 shows the Von Mises stress distribution of the beam after bending, together with the Von Mises stress and strain distributions of the embedded RVEs at two positions as indicated in the figure. Due to the complex boundary and loading conditions imposed, the stress distribution of the beam is non-uniform. The highest stress (563 MPa) appears at position P1. From the stress distribution of the embedded RVE at this position it can be seen that the distribution in the magnitude of the micromechanical stresses is much wider than typically observed at the macroscale. As expected, the martensite regions are carrying much higher stresses than the soft ferrite grains, caused by the strong microstructural stress partitioning between the two zones. Correspondingly the strain distribution of the embedded RVE reveals that the ferrite grains carry most of the micromechanical deformation, and banded zones with high strain localization appear in the ferrite regions near to the martensite grains. As a comparison to the RVE embedded at position P1, the RVE embedded at position P2 has similar strain and stress distributions while their magnitudes are much lower.

This example shows a main advantage of employing a full-field CP model in the multiscale framework. It reveals that detailed microstructure-scale effects such as stress and strain partitioning between hard and soft regions can be well captured as well as their homogenized response at the macro scale. Based on the present framework, it is also possible to integrate damage models at both, the mesoscale constitutive formulation and at the macroscale in future so that failure of components can be modeled starting from microstructurally small cracks up to macroscopic fracture. As damage nucleation and crack growth depend substantially on microstructure, the current full-field model is a very well suited approach to reflect the influence of microstructural on micromechanics and
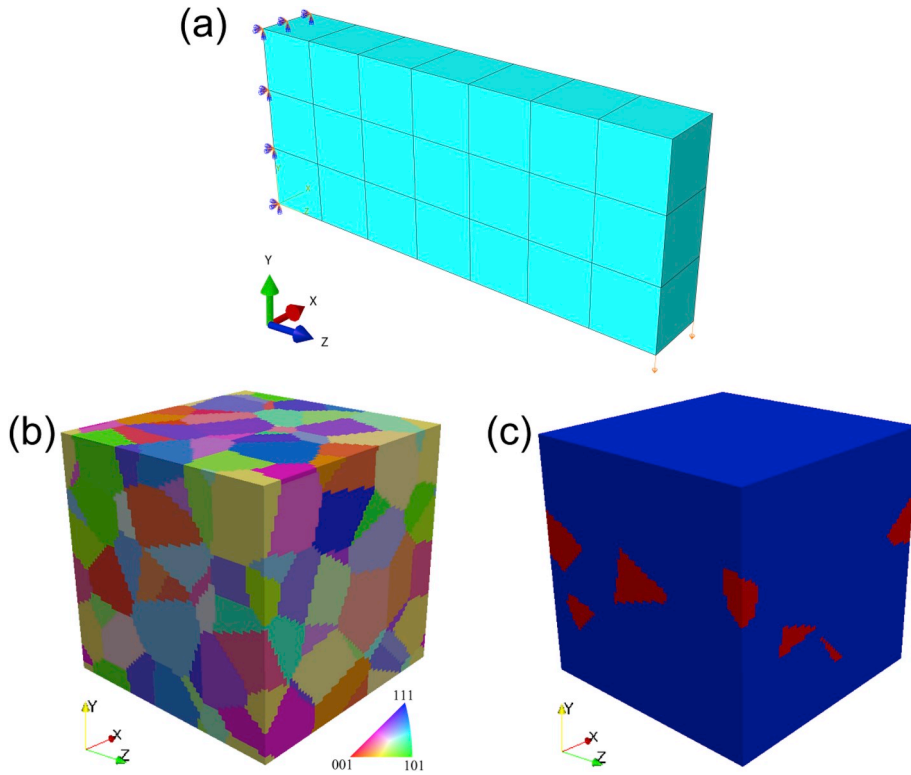
Fig. 13. (a) FEM model used for a beam bending simulation. (b) Artificial dual phase RVE microstructure with a grid resolution of $64 \times 64 \times 64$, color coded according to the IPF scheme along the Z-direction. (c) Same RVE with the ferrite colored in blue and the martensite colored in red. (For interpretation of the references to color in this figure legend, the reader is referred to the Web version of this article.)

damage evolution of materials with complex microstructures and/or high micromechanical contrast among adjacent regions.

5.5. Convergence

In the present model, the tangent stiffness matrix required by the implicit finite element is directly retrieved from the spectral-solution of the RVE by volume averaging. To study the order of convergence, three simulation cases were performed and the convergence behaviors were evaluated. In the first case, the macroscopic FE model just contains one cube element and an RVE of 1000 grains with the grid resolution of $10 \times 10 \times 10$ was embedded at the integration point. In the second case, the macroscopic FE model still contains one element while the embedded RVE was replaced by a high resolution RVE of 100 grains with a grid resolution of $64 \times 64 \times 64$. In the third case, the macroscopic FE model contains 64 ($4 \times 4 \times 4$) elements while the embedded RVE is again the low resolution RVE. Identical boundary conditions were imposed on the three FE models, i.e. the cubes ($1 \times 1 \times 1$ mm) were all uniaxially stretched in z-direction to the amount of 4% with a velocity of 0.001 mm s^{-1}. The fixed increment type boundary condition as implemented in ABAQUS was adopted. The number of increments was set to 20, which means that the simulations will be completed after 20 increments, each imposed at constant increment step size. For each increment, the strain step imposed in the FE simulation is ~ 0.002.

Table 3 lists the number of iterations at each increment for the three simulation cases. When the FE model contains one element only and an embedded RVE with grid resolution $10 \times 10 \times 10$ has been chosen, the first increment requires the most iterations compared to the other increments, as the elastic-plastic transition stage is characterized by a high nonlinearity. When the simulation is in a steady deformation stage (i.e. after 3 increments), a smaller number of iteration steps per deformation increment is required. In the second case, where the embedded RVE has $64 \times 64 \times 64$ grid resolution, both the first and second increments require each 10 iterations, a number much higher than that in the first simulation case. This observation shows that it is more difficult to converge in response regimes of high nonlinearity for a high resolution RVE. Only 1 or 2 iterations are needed in the steady deformation stage, which is comparable to the first case. In the third case where the FE model contains 64 elements, the numbers of iterations required for both the initial elastic-plastic transition stage and the steady deformation stage are higher than those in the case where the FE model only contains one element. This result reveals that it is obviously more difficult to converge for FE models with an increasing number of elements. Despite this, a decreasing tendency in the number of iterations required can still be observed.

Fig. 15 depicts the errors versus the corresponding iterations as well as the order of convergence for the selected increments for all three simulation scenarios. The error at each iteration step is defined as the norm of the difference between the sought strain increment
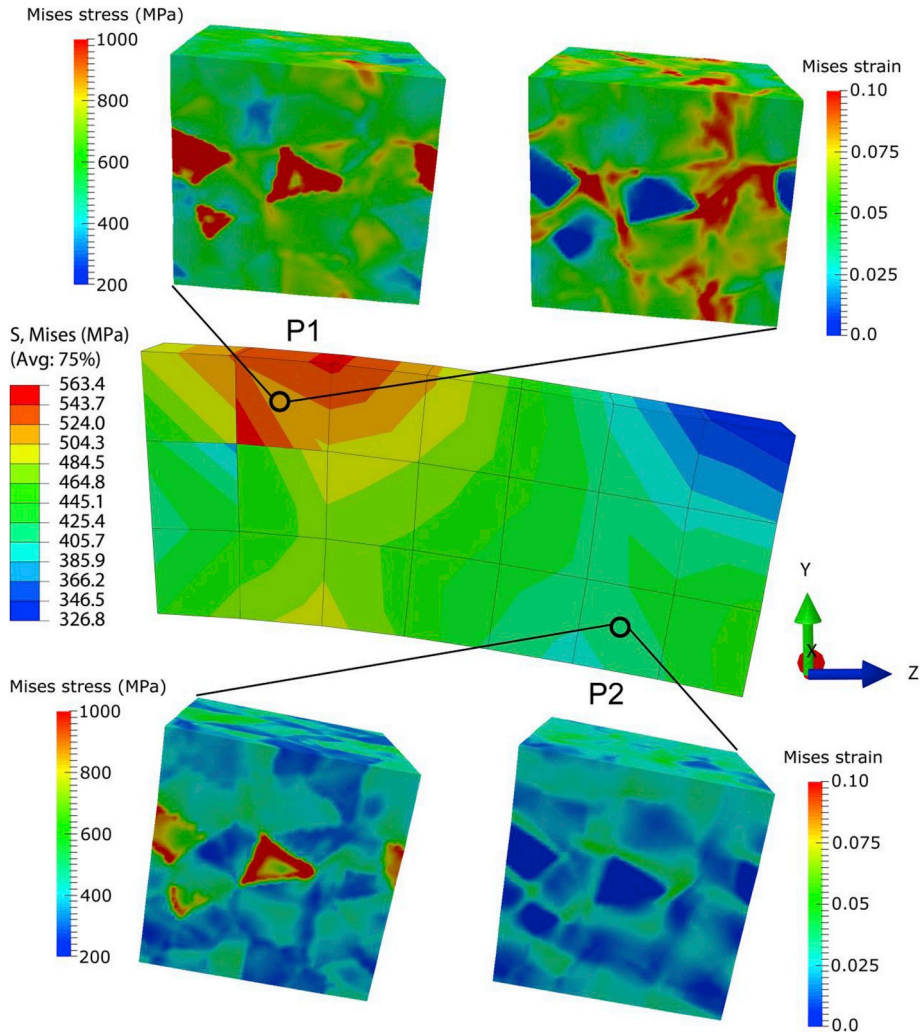
Fig. 14. Fully integrated ABAQUS-DAMASK simulation of beam bending with high lattice resolution for a dual-phase steel RVE: Distribution of the Von Mises stress, together with the Von Mises stress and Von Mises strain distributions of the embedded RVEs at the two positions indicated.

and the current guess of the strain increment. Here the sought strain increment is considered to be the finally converged one. The order of convergence is estimated following the method described in (Zecevic et al., 2017). It can be seen that it has an order of only ~0.7 for two cases, while a linear convergence is achieved for the other cases investigated. The convergence speed is acceptable in the present work, and finding a better expression of the tangent stiffness matrix for full-field homogenization to improve the order of convergence remains to be pursued in future work.
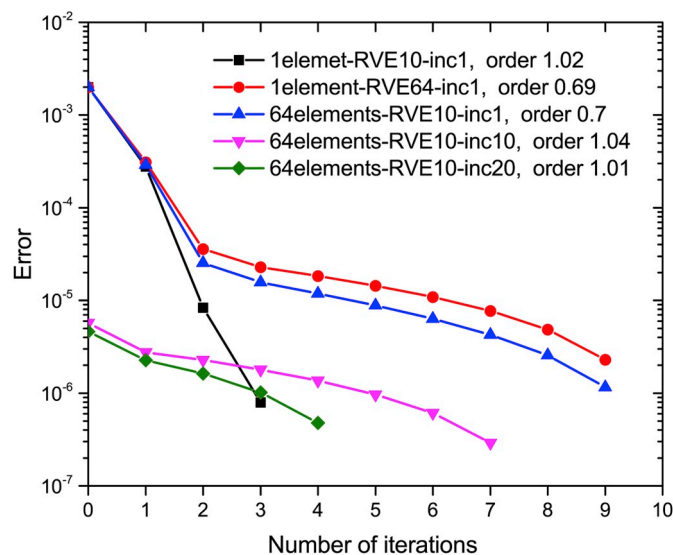
6. Conclusions

In this paper we present a physics- and mechanism-based multiscale model for polycrystal mechanics by embedding a full-field crystal plasticity model in an implicit FE framework. The spectral solver based on a FFT solution method as included in the free modeling package DAMASK is employed to provide a full-field solution for the crystal plasticity boundary condition problem according to the constraints prescribed at every forming instant by the mesoscale FE model. Simple volume averaging is used to provide the stress response and the stiffness matrix of the embedded RVE to each integration point of the macroscale FE model. The FE-FFT model was validated by reproducing the results of the stand-alone DAMASK model applied to cases of simple tension, simple compression, and simple shear on an FCC polycrystal. Four illustrative examples were presented to show the capabilities of the model in practical application. In the first example, the multiscale model successfully captures the strain heterogeneity of an FCC plate compressed by a round rigid die, as well as the deformed microstructures represented by the shapes of the embedded RVEs and corresponding textures. In the second example, the multiscale model successfully captures the stress distribution asymmetry of a compressed cylinder by employing multiple statistical and different grain-sized RVEs. In the third example, the multiscale model successfully captures the geometrical changes of highly textured HCP bars in four-point bending tests with the through-thickness directions (of the original plate

Table 3
Number of iterations at each increment.

Increment number	Number of iterations		64 elements
	1 element		
	1000grains10 × 10 × 10	100grains64 × 64 × 64	1000grains10 × 10 × 10
1	4	10	10
2	3	10	10
3	3	4	6
4	2	2	8
5	1	2	9
6	1	1	9
7	2	1	7
8	2	1	7
9	2	1	8
10	2	1	8
11	2	1	7
12	2	1	5
13	2	1	4
14	2	1	2
15	2	1	2
16	1	1	3
17	1	1	3
18	1	2	3
19	1	1	4
20	1	1	5

Fig. 15. Error versus number of iterations. 1element-RVE10-inc1: the 1st increment of the one-element FE simulation in which the embedded RVE has a grid resolution of $10 \times 10 \times 10$; 1element-RVE64-inc1: the 1st increment of the one-element FE simulation in which the embedded RVE has a grid resolution of $64 \times 64 \times 64$; 64element-RVE10-inc1: the 1st increment of the 64-element FE simulation in which the embedded RVE has a grid resolution of $10 \times 10 \times 10$; 64element-RVE10-inc10: the 10th increment of the 64-element FE simulation in which the embedded RVE has a grid resolution of $10 \times 10 \times 10$; 64element-RVE10-inc20: the 20th increment of the 64-element FE simulation in which the embedded RVE has a grid resolution of $10 \times 10 \times 10$. Y-axes is in logarithmic scale.

that the bars were cut from) orientated in the bending plane or perpendicular to that. In the fourth example, a beam bending simulation of a dual-phase steel, represented in terms of a high resolution RVE, successfully captures the stress and strain partitioning among ferrite and martensite as well as their homogenized response when analyzed for the macroscale boundary conditions.

Both a phenomenological hardening law and a dislocation density based model implemented in DAMASK have been used to provide the constitutive response at the mesoscale. As the present multiscale modeling framework is formulated very general, other advanced CP constitutive formulations implemented in DAMASK can also be used. The present model is particularly suitable for modeling materials that need to take into account complex microstructural characteristics (e.g., multiple phases, grain morphology, textures and grain size distributions), since such characteristics can only be well defined in a full-field model. It needs to be noted that the present multiscale framework is not only suitable for the simulation of the mechanical response of polycrystalline materials but

also for materials that have hierarchical or graded microstructures, as long as the underlying materials can be represented in a DAMASK RVE.

Acknowledgments

Appendix A. Notation

The tensor (or dyadic) product between two vectors is denoted as $\mathbf{T} = \mathbf{a} \otimes \mathbf{b}$ ($T_{ij} = a_i b_j$). The action of a second-order tensor upon a vector is denoted as $\mathbf{t} = \mathbf{A}\mathbf{b}$ (in components $t_i = A_{ij} b_j$) and that of a fourth-order tensor upon a second-order tensor is designated as $\mathbf{T} = \mathbb{A}:\mathbf{B}$ ($T_{ij} = A_{ijkl} B_{kl}$). The composition of 2 s-order tensors is denoted as $\mathbf{T} = \mathbf{A}\mathbf{B}$ ($T_{ij} = A_{ik} B_{kj}$). The tensor product $\mathbf{A} \boxtimes \mathbf{B}$ of 2 s-order tensors $\mathbf{A}$ and $\mathbf{B}$ is defined by $(\mathbf{A} \boxtimes \mathbf{B})\mathbf{C} := \mathbf{A}\mathbf{C}\mathbf{B}$ ($T_{ijkl} = A_{ij} \boxtimes B_{kl}$ such that $T_{ijkl}C_{kl} = A_{im}C_{mn}B_{nj}$). The transpose tensor product $\mathbf{A} \boxplus \mathbf{B}\mathbf{A} \boxplus \mathbf{B}$ of 2 s-order tensors $\mathbf{A}$ and $\mathbf{B}$ is defined by $(\mathbf{A} \boxplus \mathbf{B})\mathbf{C} := \mathbf{A}\mathbf{C}^{\mathrm{T}}\mathbf{B}$ ($T_{ijkl} = A_{ij} \boxplus B_{kl}$ such that $T_{ijkl}C_{kl} = A_{im}C_{nm}B_{nj}$). The dyadic product of 2 s-order tensors is denoted as $\mathbb{T} = \mathbf{A} \odot \mathbf{B}$ ($T_{ijkl} = A_{ij}B_{kl}$).

Appendix B. Calculation of tangent matrix

The expression for the tangent matrix appropriate to the Jaumann rate of Cauchy stress is given as

$$\mathbb{C}_{ijkl}^{\mathrm{umat}} = J^{-1}\left(F_{jm}F_{ln}\mathbb{C}_{imkn}^{\mathrm{damask}} - F_{im}P_{km}\delta_{jl}\right) + \frac{1}{2}\left(\sigma_{jl}\delta_{ik} + \sigma_{ik}\delta_{jl} + \sigma_{jk}\delta_{il} + \sigma_{il}\delta_{jk}\right) \tag{A1}$$

where $J = \det \mathbf{F}$ and δ_{jl} is the Kronecker delta. The tangent modulus $\mathbb{C}^{\mathrm{damask}} = \mathrm{d}\mathbf{P}/\mathrm{d}\mathbf{F}$ used in DAMASK is analytically derived. The first PIOLA-KIRCHHOFF stress $\mathbf{P}$ is related to the second PIOLA-KIRCHHOFF stress $\mathbf{S}$ through

$$\mathbf{P} = \mathbf{F}_{\mathrm{e}}\mathbf{S}\mathbf{F}_{\mathrm{p}}^{-\mathrm{T}} = \mathbf{F}\mathbf{F}_{\mathrm{p}}^{-1}\mathbf{S}\mathbf{F}_{\mathrm{p}}^{-\mathrm{T}} \tag{A2}$$

Therefore, the sought tangent is given as

$$\frac{\mathrm{d}\mathbf{P}}{\mathrm{d}\mathbf{F}} = \left[\mathbf{I} \boxtimes \left(\mathbf{F}_{\mathrm{p}}^{-1}\mathbf{S}\mathbf{F}_{\mathrm{p}}^{-\mathrm{T}}\right)\right] : \mathbb{I} + \left[\mathbf{F} \boxtimes \left(\mathbf{S}\mathbf{F}_{\mathrm{p}}^{-\mathrm{T}}\right)\right] : \frac{\mathrm{d}\mathbf{F}_{\mathrm{p}}^{-1}}{\mathrm{d}\mathbf{F}} + \left[\left(\mathbf{F}\mathbf{F}_{\mathrm{p}}^{-1}\right) \boxtimes \mathbf{F}_{\mathrm{p}}^{-\mathrm{T}}\right] : \frac{\mathrm{d}\mathbf{S}}{\mathrm{d}\mathbf{F}} + \left[\left(\mathbf{F}\mathbf{F}_{\mathrm{p}}^{-1}\mathbf{S}\right) \boxtimes \mathbf{I}\right] : \frac{\mathrm{d}\mathbf{F}_{\mathrm{p}}^{-1}}{\mathrm{d}\mathbf{F}} \tag{A3}$$

Using the chain-rule, $\mathrm{d}\mathbf{S}/\mathrm{d}\mathbf{F}$ can be expressed as

$$\frac{\mathrm{d}\mathbf{S}}{\mathrm{d}\mathbf{F}} = \frac{\mathrm{d}\mathbf{S}}{\mathrm{d}\mathbf{F}_{\mathrm{e}}} : \frac{\mathrm{d}\mathbf{F}_{\mathrm{e}}}{\mathrm{d}\mathbf{F}} \tag{A4}$$

where $\mathrm{d}\mathbf{S}/\mathrm{d}\mathbf{F}_{\mathrm{e}}$ is given later. $\mathrm{d}\mathbf{F}_{\mathrm{e}}/\mathrm{d}\mathbf{F}$ is expressed as

$$\frac{\mathrm{d}\mathbf{F}_{\mathrm{e}}}{\mathrm{d}\mathbf{F}} = \mathbf{I} \boxtimes \mathbf{F}_{\mathrm{p}}^{-1} + [\mathbf{F} \boxtimes \mathbf{I}] : \frac{\mathrm{d}\mathbf{F}_{\mathrm{p}}^{-1}}{\mathrm{d}\mathbf{F}} \tag{A5}$$

Considering that the time integral of the velocity gradients is approximated in an implicit manner at a fixed material state as

$$\frac{\mathbf{F}_{\mathrm{p}}(t) - \mathbf{F}_{\mathrm{p}}(t_0)}{\Delta t} = \mathbf{L}_{\mathrm{p}}(t)\mathbf{F}_{\mathrm{p}}(t) \tag{A6}$$

which results in the plastic deformation gradient at the end of the time increment being

$$\mathbf{F}_{\mathrm{p}}(t) = \left(\mathbf{I} - \Delta t\mathbf{L}_{\mathrm{p}}(t)\right)^{-1}\mathbf{F}_{\mathrm{p}}(t_0) \tag{A7}$$

from which the differential of the inverse components can be obtained as

$$\frac{\mathrm{d}\mathbf{F}_{\mathrm{p}}^{-1}}{\mathrm{d}\mathbf{F}} = -\Delta t\left[\mathbf{F}_{\mathrm{p}0}^{-1} \boxtimes \mathbf{I}\right] : \frac{\mathrm{d}\mathbf{L}_{\mathrm{p}}}{\mathrm{d}\mathbf{S}} : \frac{\mathrm{d}\mathbf{S}}{\mathrm{d}\mathbf{F}} \tag{A8}$$

where $\mathrm{d}\mathbf{L}_{\mathrm{p}}/\mathrm{d}\mathbf{S}$ is given later. By substituting Eq. (A8) into Eq. (A5) and then Eq. (A5) into Eq. (A4) it yields

$$\left[\mathbb{I} + \Delta t\frac{\mathrm{d}\mathbf{S}}{\mathrm{d}\mathbf{F}_{\mathrm{e}}} : \left(\mathbf{F}\mathbf{F}_{\mathrm{p}0}^{-1}\right) \boxtimes \mathbf{I} : \frac{\mathrm{d}\mathbf{L}_{\mathrm{p}}}{\mathrm{d}\mathbf{S}}\right] : \frac{\mathrm{d}\mathbf{S}}{\mathrm{d}\mathbf{F}} = \frac{\mathrm{d}\mathbf{S}}{\mathrm{d}\mathbf{F}_{\mathrm{e}}} : \left[\mathbf{I} \boxtimes \mathbf{F}_{\mathrm{p}}^{-1}\right] \tag{A9}$$

which is solved for $\mathrm{d}\mathbf{S}/\mathrm{d}\mathbf{F}$ and used together with Eq. (A8) to evaluate Eq. (A3).

The second PIOLA-KIRCHHOFF stress $\mathbf{S}$ is expressed as a function of its work conjugate GREEN-LAGRANGE strain $\mathbf{E}$ in the plastic configuration. Therefore its derivate is given by:

$$\frac{d\mathbf{S}}{d\mathbf{F}_e} = \frac{d\mathbf{S}}{d\mathbf{E}} : \frac{d\mathbf{E}}{d\mathbf{F}_e} \tag{A10}$$

where

$$\frac{d\mathbf{E}}{d\mathbf{F}_e} = \frac{1}{2}\left(\mathbf{F}_e^T \boxtimes \mathbf{I} + \mathbf{I} \boxplus \mathbf{F}_e\right) \tag{A11}$$

The derivative of the plastic velocity gradient $\mathbf{L}_p$ is expressed as

$$\frac{d\mathbf{L}_p}{d\mathbf{S}} = \mathbf{L}_{p,\mathbf{S}} = \sum_{\alpha} \mathbf{L}_{p,\mathbf{S}}^{\alpha} \tag{A12}$$

where the individual derivatives can be obtained as follows:

$$\mathbf{L}_{p,\mathbf{S}}^{\alpha} = \left(\dot{\gamma}^{\alpha}\mathbf{s}^{\alpha} \otimes \mathbf{n}^{\alpha}\right)_{,\mathbf{S}}$$

$$= (\mathbf{s}^{\alpha} \otimes \mathbf{n}^{\alpha}) \odot \dot{\gamma}^{\alpha}_{,\mathbf{S}}$$

$$= \frac{\partial \dot{\gamma}^{\alpha}}{\partial \tau^{\alpha}} = (\mathbf{s}^{\alpha} \otimes \mathbf{n}^{\alpha}) \odot \tau^{\alpha}_{,\mathbf{S}}$$

$$= \frac{\partial \dot{\gamma}^{\alpha}}{\partial \tau^{\alpha}} = (\mathbf{s}^{\alpha} \otimes \mathbf{n}^{\alpha}) \odot \left((\mathbf{s}^{\alpha} \otimes \mathbf{n}^{\alpha}) \cdot \mathbf{S}\right)_{,\mathbf{S}}$$

$$= \frac{\partial \dot{\gamma}^{\alpha}}{\partial \tau^{\alpha}} (\mathbf{s}^{\alpha} \otimes \mathbf{n}^{\alpha}) \odot (\mathbf{s}^{\alpha} \otimes \mathbf{n}^{\alpha}) \tag{A13}$$

References

Ardeljan, M., Beyerlein, I.J., McWilliams, B.A., Knezevic, M., 2016. Strain rate and temperature sensitive multi-level crystal plasticity model for large plastic deformation behavior: application to AZ31 magnesium alloy. Int. J. Plast. 83, 90–109.

Asaro, R.J., Needleman, A., 1985. Overview no. 42 Texture development and strain hardening in rate dependent polycrystals. Acta Metall. 33, 923–953.

Beaudoin, A.J., Mathur, K., Dawson, P., Johnson, G., 1993. Three-dimensional deformation process simulation with explicit use of polycrystal plasticity models. Int. J. Plast. 9, 833–860.

Coenen, E., Kouznetsova, V., Bosco, E., Geers, M., 2012. A multi-scale approach to bridge microscale damage and macroscale failure: a nested computational homogenization-localization framework. Int. J. Fract. 178, 157–178.

Crumbach, M., Goerdeler, M., Gottstein, G., 2006. Modelling of recrystallisation textures in aluminium alloys: I. Model set-up and integration. Acta Mater. 54, 3275–3289.

Crumbach, M., Goerdeler, M., Gottstein, G., 2006. Modelling of recrystallisation textures in aluminium alloys: II. Model performance and experimental validation. Acta Mater. 54, 3291–3306.

Dassault Systèmes, S., 2017. Abaqus 2017, Documentation. Dassault Systèmes, Rhode Island.

Delannay, L., Kalidindi, S., Van Houtte, P., 2002. Quantitative prediction of textures in aluminium cold rolled to moderate strains. Mater. Sci. Eng. A 336, 233–244.

Diehl, M., An, D., Shanthraj, P., Zaefferer, S., Roters, F., Raabe, D., 2017. Crystal plasticity study on stress and strain partitioning in a measured 3D dual phase steel microstructure. Phys. Mesomech. 20, 311–323.

Diehl, M., Shanthraj, P., Eisenlohr, P., Roters, F., 2016. Neighborhood influences on stress and strain partitioning in dual-phase microstructures. Meccanica 51, 429–441.

Eisenlohr, P., Diehl, M., Lebensohn, R.A., Roters, F., 2013. A spectral method solution to crystal elasto-viscoplasticity at finite strains. Int. J. Plast. 46, 37–53.

Eisenlohr, P., Tjahjanto, D., Hochrainer, T., Roters, F., Raabe, D., 2009. Texture prediction from a novel grain cluster-based homogenization scheme. Int. J. Material Form. 2, 523.

Fan, X.G., Jiang, X.Q., Zeng, X., Shi, Y.G., Gao, P.F., Zhan, M., 2018. Modeling the anisotropy of hot plastic deformation of two-phase titanium alloys with a colony microstructure. Int. J. Plast. 104, 173–195.

Feyel, F., 2003. A multilevel finite element method (FE2) to describe the response of highly non-linear structures using generalized continua. Comput. Methods Appl. Mech. Eng. 192, 3233–3244.

Feyel, F., Chaboche, J.-L., 2000. FE2 multiscale approach for modelling the elastoviscoplastic behaviour of long fibre SiC/Ti composite materials. Comput. Methods Appl. Mech. Eng. 183, 309–330.

Galán, J., Verleysen, P., Lebensohn, R., 2014. An improved algorithm for the polycrystal viscoplastic self-consistent model and its integration with implicit finite element schemes. Model. Simul. Mater. Sci. Eng. 22, 055023.

Gawad, J., Banabic, D., Van Bael, A., Comsa, D.S., Gologanu, M., Eyckens, P., Van Houtte, P., Roose, D., 2015. An evolving plane stress yield criterion based on crystal plasticity virtual experiments. Int. J. Plast. 75, 141–169.

Gawad, J., Van Bael, A., Eyckens, P., Samaey, G., Van Houtte, P., Roose, D., 2013. Hierarchical multi-scale modeling of texture induced plastic anisotropy in sheet forming. Comput. Mater. Sci. 66, 65–83.

Geers, M.G.D., Kouznetsova, V.G., Brekelmans, W.A.M., 2010. Multi-scale computational homogenization: trends and challenges. J. Comput. Appl. Math. 234, 2175–2182.

Hölscher, M., Raabe, D., Lücke, K., 1994. Relationship between rolling textures and shear textures in fcc and bcc metals. Acta Metall. Mater. 42, 879–886.

Han, F., Diehl, M., Roters, F., Raabe, D., 2019. Using Spectral-Based RVE Crystal Plasticity Simulations to Predict Yield Surface Evolution during Large Scale Forming Simulations.

He, W., Luan, B., Xin, R., Xu, J., Liu, Q., 2015. A multi-scale model for description of strain localization in friction stir welded magnesium alloy. Comput. Mater. Sci. 104, 162–171.

He, W., Zhang, S., Prakash, A., Helm, D., 2014. A hierarchical multi-scale model for hexagonal materials taking into account texture evolution during forming simulation. Comput. Mater. Sci. 82, 464–475.

Helm, D., Butz, A., Raabe, D., Gumbsch, P., 2011. Microstructure-based description of the deformation of metals: theory and application. JOM 63, 26–33.

Hosford, W.F., Fleischer, R.L., Backofen, W.A., 1960. Tensile deformation of aluminum single crystals at low temperatures. Acta Metall. 8, 187–199.

Hutchinson, J.W., 1976. Bounds and self-consistent estimates for creep of polycrystalline materials. Proc. R. Soc. Lond. 348, 101–127.

Jung, K.-H., Kim, D.-K., Im, Y.-T., Lee, Y.-S., 2013. Prediction of the effects of hardening and texture heterogeneities by finite element analysis based on the Taylor model. Int. J. Plast. 42, 120–140.

Kalidindi, S.R., 1998. Incorporation of deformation twinning in crystal plasticity models. J. Mech. Phys. Solids 46, 267–290.

Kalidindi, S.R., Bronkhorst, C.A., Anand, L., 1992. Crystallographic texture evolution in bulk deformation processing of FCC metals. J. Mech. Phys. Solids 40, 537–569.

Kaschner, G., Bingert, J., Liu, C., Lovato, M., Maudlin, P., Stout, M., Tomé, C., 2001. Mechanical response of zirconium—II. Experimental and finite element analysis of bent beams. Acta Mater. 49, 3097–3108.

Knezevic, M., Crapps, J., Beyerlein, I.J., Coughlin, D.R., Clarke, K.D., McCabe, R.J., 2016. Anisotropic modeling of structural components using embedded crystal plasticity constructive laws within finite elements. Int. J. Mech. Sci. 105, 227–238.

Knezevic, M., Lebensohn, R.A., Cazacu, O., Revil-Baudard, B., Proust, G., Vogel, S.C., Nixon, M.E., 2013. Modeling bending of α-titanium with embedded polycrystal plasticity in implicit finite elements. Mater. Sci. Eng. A 564, 116–126.

Knezevic, M., McCabe, R.J., Lebensohn, R.A., Tomé, C.N., Liu, C., Lovato, M.L., Mihaila, B., 2013. Integration of self-consistent polycrystal plasticity with dislocation density based hardening laws within an implicit finite element framework: application to low-symmetry metals. J. Mech. Phys. Solids 61, 2034–2046.

Kochmann, J., Ehle, L., Wulfinghoff, S., Mayer, J., Svendsen, B., Reese, S., 2018. Efficient Multiscale FE-FFT-Based Modeling and Simulation of Macroscopic Deformation Processes with Non-linear Heterogeneous Microstructures, Multiscale Modeling of Heterogeneous Structures. Springer, pp. 129–146.

Kochmann, J., Wulfinghoff, S., Ehle, L., Mayer, J., Svendsen, B., Reese, S., 2018. Efficient and accurate two-scale FE-FFT-based prediction of the effective material behavior of elasto-viscoplastic polycrystals. Comput. Mech. 61, 751–764.

Kochmann, J., Wulfinghoff, S., Reese, S., Mianroodi, J.R., Svendsen, B., 2016. Two-scale FE–FFT- and phase-field-based computational modeling of bulk microstructural evolution and macroscopic material behavior. Comput. Methods Appl. Mech. Eng. 305, 89–110.

Kouznetsova, V., Brekelmans, W., Baaijens, F., 2001. An approach to micro-macro modeling of heterogeneous materials. Comput. Mech. 27, 37–48.

Kouznetsova, V., Geers, M.G., Brekelmans, W.M., 2002. Multi-scale constitutive modelling of heterogeneous materials with a gradient-enhanced computational homogenization scheme. Int. J. Numer. Methods Eng. 54, 1235–1260.

Kouznetsova, V.G., Geers, M.G.D., 2008. A multi-scale model of martensitic transformation plasticity. Mech. Mater. 40, 641–657.

Kouznetsova, V.G., Geers, M.G.D., Brekelmans, W.A.M., 2004. Multi-scale second-order computational homogenization of multi-phase materials: a nested finite element solution strategy. Comput. Methods Appl. Mech. Eng. 193, 5525–5550.

Larsson, F., Runesson, K., 2011. On two-scale adaptive FE analysis of micro-heterogeneous media with seamless scale-bridging. Comput. Methods Appl. Mech. Eng. 200, 2662–2674.

Lebensohn, R.A., 2001. N-site modeling of a 3D viscoplastic polycrystal using fast Fourier transform. Acta Mater. 49, 2723–2737.

Lebensohn, R.A., Tomé, C., 1993. A self-consistent anisotropic approach for the simulation of plastic deformation and texture development of polycrystals: application to zirconium alloys. Acta Metall. Mater. 41, 2611–2624.

Lin, J., Yang, J., 1999. GA-based multiple objective optimisation for determining viscoplastic constitutive equations for superplastic alloys. Int. J. Plast. 15, 1181–1196.

Lu, X., Zhang, X., Shi, M., Roters, F., Kang, G., Raabe, D., 2019. Dislocation mechanism based size-dependent crystal plasticity modeling and simulation of gradient nano-grained copper. Int. J. Plast. 113, 52–73.

Ma, A., Roters, F., 2004. A constitutive model for fcc single crystals based on dislocation densities and its application to uniaxial compression of aluminium single crystals. Acta Mater. 52, 3603–3612.

Mathur, K.K., Dawson, P.R., 1989. On modeling the development of crystallographic texture in bulk forming processes. Int. J. Plast. 5, 67–94.

Miehe, C., Schotte, J., Lambrecht, M., 2002. Homogenization of inelastic solid materials at finite strains based on incremental minimization principles. Application to the texture analysis of polycrystals. J. Mech. Phys. Solids 50, 2123–2167.

Miehe, C., Schröder, J., Schotte, J., 1999. Computational homogenization analysis in finite plasticity Simulation of texture development in polycrystalline materials. Comput. Methods Appl. Mech. Eng. 171, 387–418.

Molinari, A., Canova, G., Ahzi, S., 1987. A self consistent approach of the large deformation polycrystal viscoplasticity. Acta Metall. 35, 2983–2994.

Moulinec, H., Suquet, P., 1998. A numerical method for computing the overall response of nonlinear composites with complex microstructure. Comput. Methods Appl. Mech. Eng. 157, 69–94.

Prakash, A., Nöhring, W.G., Lebensohn, R.A., Höppel, H.W., Bitzek, E., 2015. A multiscale simulation framework of the accumulative roll bonding process accounting for texture evolution. Mater. Sci. Eng. A 631, 104–119.

Raabe, D., 1995. Simulation of rolling textures of bcc metals considering grain interactions and crystallographic slip on {110},{112} and {123} planes. Mater. Sci. Eng. A 197, 31–37.

Raabe, D., Zhao, Z., Mao, W., 2002. On the dependence of in-grain subdivision and deformation texture of aluminum on grain interaction. Acta Mater. 50, 4379–4394.

Reis, F.J.P., Andrade Pires, F.M., 2013. An adaptive sub-incremental strategy for the solution of homogenization-based multi-scale problems. Comput. Methods Appl. Mech. Eng. 257, 164–182.

Roters, F., Diehl, M., Shanthraj, P., Eisenlohr, P., Reuber, C., Wong, S.L., Maiti, T., Ebrahimi, A., Hochrainer, T., Fabritius, H.O., Nikolov, S., Friák, M., Fujita, N., Grilli, N., Janssens, K.G.F., Jia, N., Kok, P.J.J., Ma, D., Meier, F., Werner, E., Stricker, M., Weygand, D., Raabe, D., 2019. Damask – the Düsseldorf Advanced Material Simulation Kit for modeling multi-physics crystal plasticity, thermal, and damage phenomena from the single crystal up to the component scale. Comput. Mater. Sci. 158, 420–478.

Roters, F., Eisenlohr, P., Hantcherli, L., Tjahjanto, D.D., Bieler, T.R., Raabe, D., 2010. Overview of constitutive laws, kinematics, homogenization and multiscale methods in crystal plasticity finite-element modeling: theory, experiments, applications. Acta Mater. 58, 1152–1211.

Segurado, J., Lebensohn, R.A., Llorca, J., Tomé, C.N., 2012. Multiscale modeling of plasticity based on embedding the viscoplastic self-consistent formulation in implicit finite elements. Int. J. Plast. 28, 124–140.

Shanthraj, P., Eisenlohr, P., Diehl, M., Roters, F., 2015. Numerically robust spectral methods for crystal plasticity simulations of heterogeneous materials. Int. J. Plast. 66, 31–45.

Smit, R., Brekelmans, W., Meijer, H., 1998. Prediction of the mechanical behavior of nonlinear heterogeneous systems by multi-level finite element modeling. Comput. Methods Appl. Mech. Eng. 155, 181–192.

Spahn, J., Andrä, H., Kabel, M., Müller, R., 2014. A multiscale approach for modeling progressive damage of composite materials using fast Fourier transforms. Comput. Methods Appl. Mech. Eng. 268, 871–883.

Tasan, C.C., Diehl, M., Yan, D., Bechtold, M., Roters, F., Schemmann, L., Zheng, C., Peranio, N., Ponge, D., Koyama, M., 2015. An overview of dual-phase steels: advances in microstructure-oriented processing and micromechanically guided design. Annu. Rev. Mater. Res. 45, 391–431.

Tasan, C.C., Diehl, M., Yan, D., Zambaldi, C., Shanthraj, P., Roters, F., Raabe, D., 2014. Integrated experimental–simulation analysis of stress and strain partitioning in multiphase alloys. Acta Mater. 81, 386–400.

Tasan, C.C., Hoefnagels, J.P., Diehl, M., Yan, D., Roters, F., Raabe, D., 2014. Strain localization and damage in dual phase steels investigated by coupled in-situ deformation experiments and crystal plasticity simulations. Int. J. Plast. 63, 198–210.

Taylor, G.I., 1938. Plastic strain in metals. J. Inst. Met. 62, 307–324.

Temizer, İ., Wriggers, P., 2008. On the computation of the macroscopic tangent for multiscale volumetric homogenization problems. Comput. Methods Appl. Mech. Eng. 198, 495–510.

Temizer, İ., Wriggers, P., 2011. An adaptive multiscale resolution strategy for the finite deformation analysis of microheterogeneous structures. Comput. Methods Appl. Mech. Eng. 200, 2639–2661.

Tikhovskiy, I., Raabe, D., Roters, F., 2006. Simulation of the deformation texture of a 17%Cr ferritic stainless steel using the texture component crystal plasticity finite element method considering texture gradients. Scr. Mater. 54, 1537–1542.

Tikhovskiy, I., Raabe, D., Roters, F., 2008. Simulation of earing of a 17% Cr stainless steel considering texture gradients. Mater. Sci. Eng. A 488, 482–490.

Tjahjanto, D., Eisenlohr, P., Roters, F., 2009. A novel grain cluster-based homogenization scheme. Model. Simul. Mater. Sci. Eng. 18, 015006.

Tjahjanto, D., Eisenlohr, P., Roters, F., 2009. Relaxed grain cluster (RGC) homogenization scheme. Int. J. Material Form. 2, 939–942.

Tjahjanto, D.D., Eisenlohr, P., Roters, F., 2015. Multiscale deep drawing analysis of dual-phase steels using grain cluster-based RGC scheme. Model. Simul. Mater. Sci. Eng. 23, 045005.

Tomé, C., Maudlin, P., Lebensohn, R., Kaschner, G., 2001. Mechanical response of zirconium—I. Derivation of a polycrystal constitutive law and finite element analysis. Acta Mater. 49, 3085–3096.

Turner, P.A., Tomé, C.N., 1994. A study of residual stresses in Zircaloy-2 with rod texture. Acta Metall. Mater. 42, 4143–4153.

Van Bael, A., Eyckens, P., Gawad, J., Samaey, G., Roose, D., Van Houtte, P., 2010. Evolution of crystallographic texture and mechanical anisotropy during cup drawing. Steel Res. Int. 81, 1392–1395.

Van Houtte, P., Delannay, L., Kalidindi, S., 2002. Comparison of two grain interaction models for polycrystal plasticity and deformation texture prediction. Int. J. Plast. 18, 359–377.

Van Houtte, P., Delannay, L., Samajdar, I., 1999. Quantitative prediction of cold rolling textures in low-carbon steel by means of the LAMEL model. Texture, Stress, Microstruct. 31, 109–149.

Van Houtte, P., Kanjarla, A.K., Van Bael, A., Seefeldt, M., Delannay, L., 2006. Multiscale modelling of the plastic anisotropy and deformation texture of polycrystalline materials. Eur. J. Mech. A Solid. 25, 634–648.

Van Houtte, P., Li, S., Seefeldt, M., Delannay, L., 2005. Deformation texture prediction: from the Taylor model to the advanced Lamel model. Int. J. Plast. 21, 589–624.

Walde, T., Riedel, H., 2007. Modeling texture evolution during hot rolling of magnesium alloy AZ31. Mater. Sci. Eng. A 443, 277–284.

Walde, T., Riedel, H., 2007. Simulation of earing during deep drawing of magnesium alloy AZ31. Acta Mater. 55, 867–874.

Wang, D., Diehl, M., Roters, F., Raabe, D., 2018. On the role of the collinear dislocation interaction in deformation patterning and laminate formation in single crystal plasticity. Mech. Mater. 125, 70–79.

Wong, S.L., Madivala, M., Prahl, U., Roters, F., Raabe, D., 2016. A crystal plasticity model for twinning- and transformation-induced plasticity. Acta Mater. 118, 140–151.

Zecevic, M., Beyerlein, I.J., Knezevic, M., 2017. Coupling elasto-plastic self-consistent crystal plasticity and implicit finite elements: applications to compression, cyclic tension-compression, and bending to large strains. Int. J. Plast. 93, 187–211.

Zecevic, M., Beyerlein, I.J., McCabe, R.J., McWilliams, B.A., Knezevic, M., 2016. Transitioning rate sensitivities across multiple length scales: microstructure-property relationships in the Taylor cylinder impact test on zirconium. Int. J. Plast. 84, 138–159.

Zecevic, M., Knezevic, M., 2017. Modeling of sheet metal forming based on implicit embedding of the elasto-plastic self-consistent formulation in shell elements: application to cup drawing of AA6022-T4. JOM 69, 922–929.

Zecevic, M., Knezevic, M., 2018. A new visco-plastic self-consistent formulation implicit in dislocation-based hardening within implicit finite elements: application to high strain rate and impact deformation of tantalum. Comput. Methods Appl. Mech. Eng. 341, 888–916.

Zecevic, M., Knezevic, M., 2019. An implicit formulation of the elasto-plastic self-consistent polycrystal plasticity model and its implementation in implicit finite elements. Mech. Mater. 136, 103065.

Zecevic, M., McCabe, R.J., Knezevic, M., 2015. A new implementation of the spectral crystal plasticity framework in implicit finite elements. Mech. Mater. 84, 114–126.

Zecevic, M., McCabe, R.J., Knezevic, M., 2015. Spectral database solutions to elasto-viscoplasticity within finite elements: application to a cobalt-based FCC superalloy. Int. J. Plast. 70, 151–165.

Zhang, H., Diehl, M., Roters, F., Raabe, D., 2016. A virtual laboratory using high resolution crystal plasticity simulations to determine the initial yield surface for sheet metal forming operations. Int. J. Plast. 80, 111–138.

Zhang, H., Liu, J., Sui, D., Cui, Z., Fu, M., 2018. Study of microstructural grain and geometric size effects on plastic heterogeneities at grain-level by using crystal plasticity modeling with high-fidelity representative microstructures. Int. J. Plast. 100, 69–89.

Zhao, Z.-s., Mao, W.-m., Roters, F., Raabe, D., 2004. A texture optimization study for minimum earing in aluminium by use of a texture component crystal plasticity finite element method. Acta Mater. 52, 1003–1012.